Delft University of Technology

A lattice boltzmann approach to surfactant-laden emulsions

Mukherjee, Siddhartha; Berghout, Pieter; Van den Akker, Harry E.A.

Important note
To cite this publication, please use the final published version (if applicable).
Please check the document version above.

A Lattice Boltzmann Approach to Surfactant-Laden Emulsions

Siddhartha Mukherjee* ⬤

Dept. of Chemical Engineering, Faculty of Applied Sciences Section of Transport Phenomena, Delft University of Technology, 2629 HZ, Delft, The Netherlands

Pieter Berghout

Dept. of Mechanical, Aeronautical and Biomedical Engineering, Faculty of Science and Engineering, Bernal Institute, School of Engineering, University of Limerick Limerick, Ireland

Harry E.A. Van den Akker ⬤

Dept. of Chemical Engineering, Faculty of Applied Sciences Section of Transport Phenomena, Delft University of Technology, 2629 HZ, Delft, The Netherlands

Dept. of Mechanical, Aeronautical and Biomedical Engineering, Faculty of Science and Engineering, Bernal Institute, School of Engineering, University of Limerick Limerick, Ireland

We present a pseudopotential lattice Boltzmann method to simulate liquid–liquid emulsions with a slightly soluble surfactant. The model is investigated in 2-D, over a wide parameter space for a single, stationary, immiscible droplet, and surface tension reduction by up to 15% is described in terms of a surfactant strength Λ (which roughly follows a Langmuir isotherm). The basic surfactant model is shown to be insufficient for arresting phase segregation—which is then achieved by changing the liquid–liquid interaction strength locally as a function of the surfactant density. 3-D spinodal decomposition (phase separation) is simulated, where the surfactant is seen to adapt rapidly to the evolving interfaces. Finally, for pendent droplet formation in an immiscible liquid, the addition of surfactant is shown to alter the droplet-size distribution and dynamics of newly formed droplets. © 2018 The Authors. *AIChE Journal* published by Wiley Periodicals, Inc. on behalf of American Institute of Chemical Engineers. *AIChE J*, 00: 000–000, 2018
Keywords: multiphase flow, lattice Boltzmann, pseudopotential, surfactants, emulsions

Introduction

During the last two decades or so, computer aided process engineering tools have started playing an important role in designing, debottlenecking, and optimizing both individual process devices and complete process plants. Part of this development is due to the evolution of computational fluid dynamics (CFD) for both single-phase and multiphase systems including various transport processes and chemical reactions. This, along with computational power rocketing according to Moore's law[1] has made massively parallel simulations possible, bridging the gap between detailed flow dynamics and designing for large-scale equipment.

Despite the diverse advances in the development of flow simulation techniques, conventional Finite Volume (FV) based solvers, introduced as early as the 1970s (see Patankar and Spalding[2]), still

dominate the field to an extent that virtually all commercial CFD software is rooted in FV. Much to its disadvantage, the chemical engineering community seems to keep overlooking the promises of the lattice Boltzmann (LB) method, a strong alternative to FV.

LB is a mesoscopic approach to continuum fluid mechanics, which can be used to simulate flows obeying the Navier–Stokes equations at a fraction of the computational cost of FV, particularly for (massively) parallel flow simulations. Eggels[3] and Derksen and Van den Akker[4,5] introduced the LB technique into the realm of engineering fluid mechanics. The result was a long series of papers reporting about LB based Large Eddy Simulations (LESs) in various flow devices. Most of these simulations, as well as some Direct Numerical Simulations (DNSs) see[6,7] were simply impossible using the conventional FV technique (on the platforms of the time and under the pertinent conditions).

Multiphase simulation methods can be broadly classified as Euler–Euler or Euler-Lagrangian methods. In the Euler–Euler method, fluids and particles are all treated as continua and are represented by their respective volume fractions at each grid cell of the simulation. These simulations do not resolve phase interfaces. Euler–Lagrangian methods, confined to dilute particle systems, track the individual particles which can be either point particles or finite sized. In the case of RANS-based simulations or LESs, the flow between these particles is not

---

resolved. DNS simulations, such as Ten Cate et al.[8] for solid particles in a turbulent liquid flow, and Derksen and Van Den Akker[9] for a turbulent emulsion, do resolve the flow between the particles. LB also emerges as a robust technique for simulating multiphase flows, at par with FV based solvers.[10-12] While particle laden flows like fluidized beds, suspensions, and colloids have their own dedicated LB models exploiting immersed boundary conditions for reproducing the detailed interaction of fluid and moving and revolving particles,[8,13-16] we will focus here on liquid–liquid systems.

Emulsions

This article aims at simulating the hydrodynamic behavior of emulsions which are crucial to various industries, ranging from cosmetics, biotechnology, and food processing to the oil and gas industry. Most (FV) simulations of dense droplet systems incorporate Population Balance modeling[17] which relies heavily on empirical relations drawn from experimental data. Although useful, this method suffers from the strong limitations of experimentally studying emulsions, due to their highly 3-D spatio-temporal flow characteristics around evolving interfaces; in addition, emulsions are inherently opaque to optical measurement techniques. Here, the unprecedented details unraveled by flow resolving simulation techniques can be telling.

Due to a dense droplet population, emulsions have a multitude of interfaces separating the two liquids, and the stability of these interfaces is crucial to the stability of the emulsion—that is, if they rupture leading to droplet coalescence, the two fluids would entirely separate. Emulsion stability is greatly altered by the presence of surfactants, which are surface active molecules preferentially adhering to interfaces. For instance, in enhanced oil recovery, steam is often used to mobilize the oil, which can cause emulsification facilitated by the presence of naturally occurring[18] or artificially added surfactants.[19] Surfactant stabilized emulsions are also used to transport highly viscous crude oils, whereafter these emulsions need to be destabilized to separate the oil and water phases.[20]

Surfactant induced phenomena include drag enhancement on droplets, inhibition of coalescence, modification of interfacial boundary conditions, and Marangoni flow due to (flow induced) surface tension gradients. None of these effects are present in commercial multiphase flow solvers, while various academic attempts have been made to account for these as shall be described below. While it is rare to encounter pure fluids in real life, it is exceedingly difficult to turn numerical fluids impure. Bridging the divide between real fluid mixtures and simulations is the main goal of the research described in this article which focuses on LB based detailed simulations of emulsions allowing for deformation, coalescence, and breakup of droplets while accounting for surfactants.

Simulating surfactant dynamics along with hydrodynamics is a complex problem, aggravated by the fact that the surfactant adsorption and desorption kinetics occurs at the microscale. Ionic surfactants interact directly with the electric double layer formed at the interface, also called the *Debye layer*, the thickness of which is $\mathcal{O}(10^{-10}-10^{-7}\,m)$.[21] Surfactants can also form complex aggregates like micelles and lamellae above a critical concentration. These phenomena at the microscale can influence the dynamics of droplets and bubbles, which can be of the scale $\mathcal{O}(10^{-6}\,m)$ in emulsions, or of larger scales around $\mathcal{O}(10^{-3}-10^{-1}\,m)$ in bubble columns. These scales, when dealing with a physically relevant flow, are separated by $8-10$ orders of magnitude. This poses an immense difficulty

that has to be overcome when simulating such systems. Prior research has sought to resolve this by making reductionist assumptions regarding the nature of a surfactant, limiting its essential features. After all, simulating surfactant molecules explicitly while resolving flow is not feasible, nor necessary if surfactant behavior is aptly modeled when one is solely interested in the macroscopic hydrodynamics. Below, we briefly highlight some work done in this direction.

FV based techniques

Among the FV based techniques, Stone and Leal[22] and Eggleton et al.[23] used a boundary integral method to study the breakup of a single surfactant-laden droplet. Several studies employed the Volume of Fluid (VOF) method with an insoluble surfactant confined to the interface, see for example, Renardy et al.,[24] Drumright-Clarke and Renardy,[25] James and Lowengrub ,[26] Martin and Blanchette.[27] Xu et al.[28] followed a similar approach with the Level-Set (LS) method, also used recently by De Langavant et al.[29] and applied to sheared droplet breakup. Other methods include the front tracking for interfacial and bulk surfactant transport,[30] and the arbitrary-Euler–Lagrangian approach for interface tracking by Dieter-Kissling et al.[31] applied to droplet formation in the presence of surfactant mixtures. These techniques are well suited for the particular problems being studied, and can give very accurate predictions.

The domain of single droplet dynamics, however, is far from the typical systems encountered in emulsion research. Further, there is no simple extrapolation from the idealized problems studied here to dynamic multiple droplet flows. The constant interface tracking and reconstruction used in these methods becomes challenging once multiple bubbles and droplets are simulated, more so when they can undergo coalescence and breakup, when these techniques become prohibitively expensive and complicated, if not completely unfeasible. We do not discredit these techniques at all, for they can very accurately simulate single droplets, even at very high density and viscosity ratios. However, when looking at realistic emulsions, the capabilities offered by LB far outweight the FV state-of-the-art.

LB based techniques

A few LB techniques have also been introduced, and these seem more aptly suited for simulating emulsions than the FV techniques as shall become evident. In the Pseudopotential (PP) LB model, introduced by Shan and Chen,[32,33] adding molecular interactions between particle distributions at the meso-scale can simulate spontaneous phase separation. Many researchers embarked on this concept with the view of describing two-phase systems,[34] also in our research group.[35-37] As multiple interfaces do not need to be tracked, captured and/or reconstructed, the PP-LB method is computationally very attractive.[12]

Contrary to the bottom–up PP method, there is the top–down free-energy method for simulating multiphase flows in LB.[38,39] Simulations using this approach start with a free-energy functional with the intended thermodynamics, which is then used to derive other physical quantities, making these methods thermodynamically consistent by definition.[40] This method has the advantage that certain properties like surface tension and interface width can be predefined. A drawback is that the method has been found to be almost three times more computationally expensive than other comparable LB methods.[41]

Focusing on emulsion like systems with two immiscible fluid components, Chen et al.,[42] Nekovee et al.[43] introduced a

multicomponent PP-LB approach where the surfactant is incorporated as a third additional component, coupled to an idealized point dipole. The dipole moment and surfactant distribution both follow the LB streaming and collision algorithm. The surfactant concentration, however, is of the same order as the other fluids, which is not always the case in physical systems. Using this model, Nekovee et al.[43] go on to confirm arrested phase segregation for high resolution 2-D simulations on the addition of an active surfactant. They also observe the formation of lamellae above the critical micellar concentration (CMC), not seen in past simulations, which they ascribe to the inclusion of the dipole orientation in their model. Skartlien et al.[44] demonstrated the dynamic surface tension behavior of this model and show how the parameters can be tuned to resemble a physical surfactant like *Exxsol D80* and *Span 80*.

Furtado and Skartlien[45] derived the free energy form of the Chen et al.[42] model from underlying kinetic theory principles. Including short and long range interactions, they also show an inhibition of coalescence. Note that coalescence inhibition alone can also be simulated *without* surfactants using alternate techniques (like charge on the droplets[46] or mid-range repulsive interaction forces[47]), but Marangoni flows cannot. Skartlien et al.[48] used this model to study surfactant stabilized emulsions in a quasi-turbulent flow which is induced by the conversion of surface energy to kinetic energy during phase segregation and Skartlien et al.[49] investigated droplet-size distribution in weakly turbulent surfactant laden emulsions. Free-energy method based models to simulate surfactant stabilized dispersions have also been proposed. Lamura et al,[50] used a Ginzburg-Landau based model to show the spontaneous formation of lamellae in surfactant laden oil–water systems due to surface tension reduction. A similar approach was used by Van der Sman and Van der Graaf[51] to show Ward-Tordai like kinetics of surfactant adsorption. This method was further developed by Tóth and Kvamme[52] to show slowed down phase segregation due to the presence of surfactants, and applied to oil, water, and asphaltene systems.[53] A thorough review of models for ionic surfactants has been presented by van der Sman and Meinders,[54] which also gives model taxonomy, distinguishing between Eulerian and Lagrangian approaches, with the various ways of simulating surfactants with different degrees of complexity that have been developed so far.

A lot of the studies using the Chen et al.,[42] Nekovee et al.[43] model have focused on the formation of exotic gyroidal structures, complex aggregates and emergent behavior in ternary systems,[55-59] which makes the model quite unique. However, the model has not been used for a wide range of multiphase flow problems where surfactant laden simulations find application. Its complexity and the extensive parameter space perhaps obscure its utility, whereby arises the need for simplification.

In this article, we propose the simplest method to incorporate soluble surfactants in a two fluid mixture by implementing a doubly repelled third surfactant component. We retain surfactant effects like surface tension reduction, and present an analysis through the corresponding parameter space. Our approach combines several other PP-LB developments, making it easy to simulate a wide range of density ratios $\mathcal{O}(1-10^3)$, different viscosity ratios between the fluids and the surfactant (which has been recently demonstrated to be an important parameter[60]), and a possibility of extension to multiple surfactants and components if required. There are several differences between our model and those suggested previously in literature,[45,52,54,57] apart from that we use the pseudopotential method while the latter employ the free-energy method. First, we ignore the dipole orientation of the surfactant (and

consequently aggregate-like behavior). Further, we simulate realistic fluids by modeling the components using nonideal equations of state. This approach allows for a wider range of density ratios between components, which shall allow for simulations of surfactant laden droplets and bubbles. We also propose modifications to our simplified surfactant model that can help simulate more complex surfactant behavior like the spontaneous formation of microemulsions which has not been presented before using LB.

Numerical Method

The lattice Boltzmann method

In this study, we use the lattice Boltzmann method (LBM), first proposed in their seminal paper by McNamara and Zanetti.[61] The Boltzmann equation, with a simplified collision term (BGK[62]), is discretized up to second order in time, space and momentum, and consequently solved on a lattice that comprises the discretization of space D and momentum Q in i and j directions respectively, and which is named D_iQ_j. The velocity space is reduced to a finite number of discrete values (i.e., Q_j), and one must have sufficient velocity directions to obey the conservation laws. Yet, for a very wide range of 2-D flows, a nine velocity set is sufficient to recover the macroscopic hydrodynamics, and 19 velocities in 3-D.[40]

As the Boltzmann equation solves for the particle distribution function, it falls within the mesoscopic compendium of fluid solvers. Consequently, it is well suited to bridge the gap between the microscopic particle scale and the macroscopic continuum scale of fluid flow by invoking mesoscopic particle interactions. This makes modeling multiphase flow phenomena conceptually simple, as with the Pseudopotential method (described shortly), and phenomena like spontaneous phase segregation, bottom–up surface tension effects and evolving interfaces are automatically captured. The spatio-temporal locality of the computations involved makes the method easily parallelizable over distributed computational units unlike conventional FV based solvers where distant units need to communicate for the pressure and velocity coupling of an iterative Navier–Stokes solver. Given these factors, the LB method has gained widespread popularity over the past decades, for both single phase and multiphase flows.[34,40]

The LB equation reads

$$f_i^\sigma(\mathbf{x} + c\mathbf{e}_i\Delta t, t + \Delta t) - f_i^\sigma(\mathbf{x}, t) = \frac{1}{\tau^s}\left(f_i^{\sigma,eq}(\mathbf{x}, t) - f_i^\sigma(\mathbf{x}, t)\right) + S_i^\sigma$$

(1)

where f_i^σ is the particle (or density) distribution function for some component σ in the discrete velocity direction i. The lattice speed c is defined as $c = \Delta x/\Delta t = 1$, implying constant kinetic energy for all equal mass particles and τ is the lattice relaxation time towards local equilibrium. S_i^σ is a source term which incorporates body forces. Most simulations in this article were carried out on a $D2Q9$ lattice, using the standard nine lattice velocities in two dimensions, $\mathbf{e}_i$, as defined below

$$\mathbf{e}_i = \begin{cases} (0,0), & i=0 \\ \left(\cos\left[\frac{(i-1)\pi}{2}\right], \sin\left[\frac{(i-1)\pi}{2}\right]\right)c, & i=1,2,3,4 \\ \sqrt{2}\left(\cos\left[\frac{(i-5)\pi}{2} + \frac{\pi}{4}\right], \sin\left[\frac{(i-5)\pi}{2} + \frac{\pi}{4}\right]\right)c, & i=5,6,7,8 \end{cases}$$

(2)

The $D3Q19$ simulations similarly utilize the standard 19 velocity 3-D lattice, which can be found described in

Krüger et al.[40] The discretized equilibrium distribution function follows from a multiscale expansion in the incompressible (low Mach number) limit of the Maxwellian[63]:

$$f_i^{\sigma,eq} = w_i \rho_\sigma \left\{ 1 + \frac{\mathbf{e}_i \cdot \mathbf{u}_\sigma}{RT} + \frac{(\mathbf{e}_i \cdot \mathbf{u}_\sigma)^2}{2(RT)^2} - \frac{\mathbf{u}_\sigma^2}{2RT} \right\} \tag{3}$$

The weight factors are $w_0 = 4/9$, $w_{1 \to 4} = 1/9$ and $w_{5 \to 8} = 1/36$. ρ_σ is the component density and follows from the zeroth moment of the distribution function:

$$\rho_\sigma = \sum_i f_i^\sigma \tag{4}$$

$\mathbf{u}_\sigma$ is the bare component velocity[40] and follows from the first moment of the distribution function:

$$\rho_\sigma \mathbf{u} = \sum_i \mathbf{e}_i f_i^\sigma + \frac{F_i \Delta t}{2} \tag{5}$$

where F_i is the force term. The lattice viscosity is related to the lattice relaxation time by

$$\nu = c_s^2(\tau - 1/2) \tag{6}$$

where the pseudosound-speed $c_s = \sqrt{RT}$ has the value $1/\sqrt{3}$ for the $D2Q9$ lattice. Details regarding the derivation of these quantities can be found in Succi.[64]

Multicomponent multiphase (MCMP) modeling

Various multiphase and multicomponent models have been proposed within the LB framework.[33,65,66] In this article, we make use of the PP-LB model. This is a bottom–up approach, where multiphase hydrodynamics emerges from particle interactions based on a mean field interparticle force. Characteristic parameters of multiphase systems like interfacial tension and the density ratio of coexisting phases, naturally emerge from the interaction between the respective fluid components. This obviates the usual requirement of solving additional equations to capture or track the interface as one has to with traditional FV methods like the Volume of Fluid, LS and so forth, and the method can be made thermodynamically consistent.[37]

In this article, we simulate three components, which are labeled as α, the high density liquid, β the low density liquid, and s the surfactant. In general, the total force $\mathbf{F}$ on a component σ is the sum of the intracomponent force $\mathbf{F}^{\sigma\sigma}$ (which is based upon an equation-of-state) and a sum of intercomponent repulsion forces $\mathbf{F}^{\sigma\bar{\sigma}}$ that can be interpreted as the force on σ due to $\bar{\sigma}$. Together these can be written as

$$\mathbf{F}^\sigma(\mathbf{x},t) = \mathbf{F}^{\sigma\sigma}(\mathbf{x},t) + \sum_{\bar{\sigma} \neq \sigma} \mathbf{F}^{\sigma\bar{\sigma}}(\mathbf{x},t) \tag{7}$$

(for instance $\mathbf{F}^\alpha = \mathbf{F}^{\alpha\alpha} + \mathbf{F}^{\alpha\beta} + \mathbf{F}^{\alpha s}$). The intercomponent interaction force $\mathbf{F}^{\sigma\bar{\sigma}}$ takes the classical Shan-Chen form.[32]

$$\mathbf{F}^{\sigma\bar{\sigma}}(\mathbf{x},t) = -G_{\sigma\bar{\sigma}}\phi_\sigma(\mathbf{x},t)c_s^2 \sum_{i=0}^{N} w\left(|\mathbf{e}_i|^2\right)\phi_{\bar{\sigma}}(\mathbf{x}+\mathbf{e}_i\Delta t,t)\mathbf{e}_i \tag{8}$$

where we sum over the nearest neighbors ($i = 0 \to 8$). Here ϕ is the pseudopotential function, and we use the component density as ϕ, while other definitions are possible. Further, $c_s^2 = 1/3$ is the lattice speed of sound, and G is the interaction strength. This force is incorporated in the source term in

Eq. 1. Note that its magnitude should not be disproportionately large, which can lead to numerical instabilities, as its upper bounds are set roughly by the magnitude of the component densities which comprise the left hand side of Eq. 1.

Table 1 gives the different interaction strengths, where a negative value gives attraction between the two components (miscibility), whereas a positive value gives repulsion (immiscibility). The surfactant is repelled by both the fluid components, and consequently is driven toward the interface. This is a highly simplified picture of the interaction of a surfactant with the two fluids. In reality, each surfactant molecule has a finite length, with a hydrophilic head and a hydrophobic tail, and it is this amphiphilic nature that drives it to seek out fluid interfaces. At a mesoscopic level, surfactants are treated as point particles, where it would seem that both fluids repel the surfactant. This approach does allow simulation of surfactants collecting at the interfaces, and reducing surface tension of the droplets as will be demonstrated. Finite size effects like steric repulsion, or formation of and interaction with electric double layers are not taken into account in the model yet. We further ignore the orientation of these molecules, also linked to the finite surfactant molecule sizes, which can lead to charge based repulsion between approaching surfactant laden interfaces. This simplified model can be used to successively incorporate features that can simulate more complex effects that are currently out of scope. We want to emphasize that the different components stream and collide on their own respective lattices such that there is no excluded volume effect, and the components only interact by means of the interaction force.

We keep the concentration of the surfactant three orders of magnitude lower than the liquid densities. This is because in real systems, the surfactant volume fraction is very low compared to the liquid components in the entire domain. Only at the interfaces, the surfactant can have high volume fractions, even close to unity at high surfactant loading. A higher average surfactant density in the domain can also cause the surfactant to also form droplets, which is not desired. However, a very low surfactant density introduces another caveat. The liquid-to-surfactant forces (i.e., $\mathbf{F}^{s\alpha}$, $\mathbf{F}^{s\beta}$) which are based upon the liquid densities become much larger than the counter acting intracomponent hard-sphere like repulsion modeled in the nonideal EOS. To overcome these instabilities, a factor S is used to scale the liquid-to-surfactant forces, as done by Skartlien et al.,[44] which makes the total force on the surfactant

$$\mathbf{F}^s = \mathbf{F}^{ss} + \frac{1}{S}\left(\mathbf{F}^{s\alpha} + \mathbf{F}^{s\beta}\right) \tag{9}$$

Note that this scaling factor can effect momentum conservation as pair-wise momentum between the liquids and

Table 1. The six intracomponent and intercomponent interaction strengths coupling the three components to each other. The exact choice of the intracomponent interaction strengths, $G_{\sigma\sigma}$, is not important as the term cancels out following Eqs. 10 and 11, with the only requirement that it be negative to keep the argument of the square root positive, hence these is fixed to -1.0. The intercomponent interaction strengths $G_{\sigma\bar{\sigma}} > 0$

	α	β	s
α	$G_{\alpha\alpha}$	$G_{\alpha\beta}$	$G_{\alpha s}$
β	$G_{\beta\alpha}$	$G_{\beta\beta}$	$G_{\beta s}$
s	$G_{s\alpha}$	$G_{s\alpha}$	G_{ss}

surfactant is not conserved when $S \neq 1$. However, in this article all simulations are performed on fully periodic domains, due to which the sum of all interparticle interactions cancels out such that global momentum is conserved, which was found to be true for all S values used in this article. Alternatives to the scaling factor would be using a higher surfactant density (while somehow avoiding the formation of surfactant droplets), or using the surfactant distribution to influence other parameters of the simulation, as will be discussed in the section on coalescence inhibition under results.

The intracomponent interaction force, $\mathbf{F}^{\sigma\sigma}$, is calculated by means of the β-Scheme.[67]

$$\mathbf{F}^{\sigma\sigma}(\mathbf{x},t) = -\beta G_{\sigma\sigma}\Psi_\sigma(\mathbf{x},t)c_s^2\sum_{i=0}^{N}w\left(|\mathbf{e}_i|^2\right)\Psi_\sigma(\mathbf{x}+\mathbf{e}_i\Delta t,t)\mathbf{e}_i - \frac{1-\beta}{2}G_{\sigma\sigma}\sum_{i=0}^{N}w\left(|\mathbf{e}_i|^2\right)\Psi_\sigma(\mathbf{x}+\mathbf{e}_i\Delta t,t)^2\mathbf{e}_i$$

(10)

With the proper choice of the weighting parameter β, the spurious velocities occurring at curved interfaces can be reduced significantly.[37] For this research, we set the weighting factor β to 1.25, as suggested by Zarghami et al.[37]

Phase separation is achieved by implementing the Carnahan-Starling (CS) equation of state (EOS). The interaction term then becomes

$$\Psi_\sigma = \sqrt{\frac{6}{G_{\sigma\sigma}}\left(\rho_\sigma RT\frac{1+b_\sigma\rho_\sigma/4+(b_\sigma\rho_\sigma/4)^2-(b_\sigma\rho_\sigma/4)^3}{(1-b_\sigma\rho_\sigma/4)^3}-a_\sigma\rho_\sigma^2-\rho c_s^2\right)}$$

(11)

where a_σ and b_σ are respectively the repulsion and attraction parameters, characteristic of the different fluid components, and are set to $a = 0.4963R^2T_c^2/p_c$ and $b = 0.18727RT_c/p_c$, R is the universal gas constant and here set to 1,[37] and T_c and p_c are respectively the critical temperature and the critical pressure of the component of interest. For $T > T_c$, only one phase exists, while for $T < T_c$, two phases coexist with a density ratio determined by the reduced temperature $T_r = T/T_c$, where the corresponding liquid and vapor densities can be calculated by means of the Maxwell construction. The physical temperature is kept the same for all components by ensuring $T = T_c^\sigma \times T_r^\sigma$ has the same value.

The force is implemented in the source term S_i^σ in Eq. 1 using the exact differencing method (EDM),[68] given as follows

$$S_i^\sigma = f_i^{eq}\left(\rho,\mathbf{u}+\frac{\mathbf{F}^\sigma\Delta t}{\rho}\right)-f_i^{eq}(\rho,\mathbf{u})$$

(12)

The pressure in the system is calculated as a sum of the individual fluid component contributions based upon their EOS, and the non ideal contributions due to intercomponent interactions.[69]

$$P = c_s^2\sum\rho_\sigma + \frac{1}{2}c_s^2\sum G_{\sigma\sigma}\Psi_\sigma^2 + \frac{1}{2}c_s^2\sum_{\sigma\neq\bar{\sigma}}G_{\sigma\bar{\sigma}}\phi_\sigma\phi_{\bar{\sigma}}$$

(13)

Note that all quantities in this study are nondimensional, though when simulating flow problems they can be mapped to physical units by keeping some nondimensional numbers (such as a Reynolds number) constant. Such a mapping was presented in Mukherjee et al.[12] for simulations of falling droplets. Lastly, we have used the massively parallel, open source lattice-Boltzmann solver Palabos in this study.[70]

Results

Validation

To validate our computer code and numerical model, we perform two sets of simulations. In the first study, we validate the thermodynamic consistency of a single component multiphase system when simulated by means of the Carnahan-Starling EOS. Within a (square) periodic box, a droplet of component α is initialized as a diffused circular region defined as

$$\rho(x,y) = \frac{\rho_l+\rho_v}{2} + \frac{\rho_l-\rho_v}{2}\left[\tanh\left(2\frac{\sqrt{(x-x_i)^2+(y-y_i)^2}-R_0}{W}\right)\right]$$

(14)

where $W = 6$ is the interface thickness, R the droplet radius, ρ_l and ρ_v are the densities of component α in the liquid and vapor phases, respectively. The domain size is $N_x = N_y = 601$ and $x_i = y_i = 301$ is the position of the center of the droplet. The respective values of the initial densities inside and outside the droplet are estimated from the Maxwell curve. The Maxwell curve dictates the coexisting densities for a component at a given reduced temperature T_r. The EOS parameters are $a = 1.0$ and $b = 4.0$, and the weighting parameter β of the β-scheme is 1.25.

All stationary droplet simulations have been performed for 20,000 iterations, to ensure that equilibrium is attained. After reaching equilibrium, the liquid and vapor densities corresponding to inside and outside of the droplet are shown in Figure 1 for various T_r values. At high T_r, where the strength of the phase separation is only moderate, we find excellent agreement with the Maxwell curve. For lower reduced temperatures, our numerical results start to deviate from the analytical curve, however only slightly. The lowest reduced temperature we can obtain is $T_r = 0.4$, with $\rho^\star = \rho_l/\rho_v = O(10^3)$. The thickness of the interface varies from roughly 8–3 lattice units [lu] as T_r is reduced from 0.96 to 0.4. These results are identical to recent literature.[12,37]

Next, we add an ideal lighter component β to validate the multicomponent, multiphase model with the Laplace law
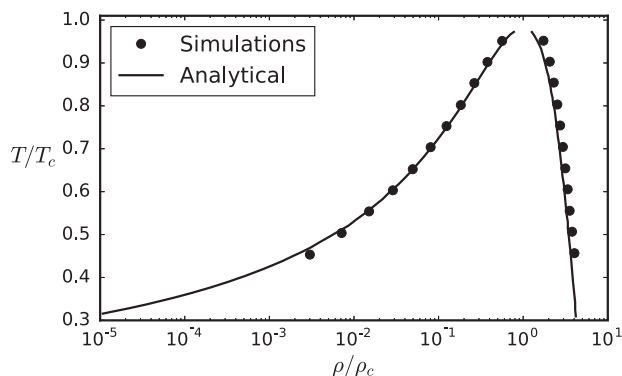

Figure 1. Analysis of thermodynamic consistency of the model by comparing simulation results to analytical solution of the Maxwell coexistence curve that gives the two fluid densities existing together at a given reduced temperature.
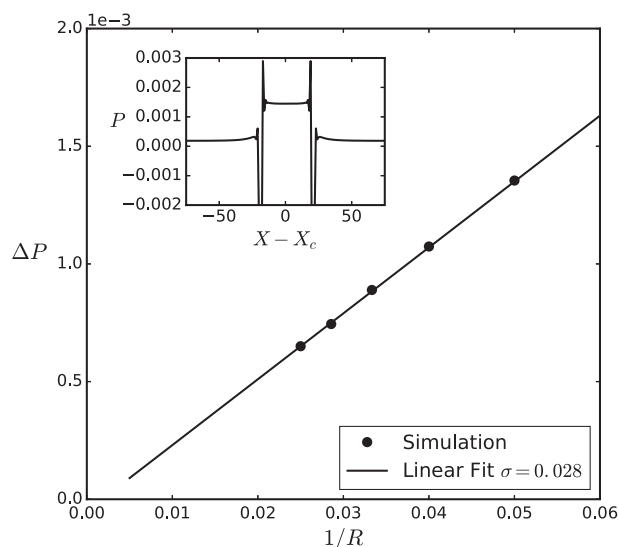
Figure 2. Laplace law validation for a multicomponent system is shown where, ΔP is the pressure difference between the center of the droplet and the edge of the domain.

Surface tension is the slope of the linear fit to ΔP over $1/R$, and is found to be $\sigma = 0.028$. The inset shows a typical pressure profile (calculated using Eq. 13) across the droplet diameter as indicated.

(Eq. 15). A stationary droplet of the non-ideal heavy component α, suspended in a quiescent lighter ideal component β is simulated in a periodic 2D domain. The initial densities for component α are $\rho_l = 0.45$, $\rho_v = 0.00007$, initialized using Eq. 14. Component β is uniformly initialized with density, $\rho = 0.00025$. Further, $T_r^\alpha = 0.52$, $\beta = 1.0$, $a = 1.0$ and $b = 4.0$. Note that the presence of component β strongly affects the phase separation of component α, such that for the same reduced temperature T_r, we find a different ρ_l/ρ_v internally within α, as compared to Figure 1. After the system has come to a steady state, we calculate the pressure difference between the center of the droplet and the edge of the domain. This is successively done for five different droplet radii R, plotted in Figure 2. Here, R is taken to be the radius of the contour level defined by $\rho_\alpha/2$, which is a point that lies inside the diffused interface at about half the interface width. It could also be defined as the distance between the center of the droplet and the point where $\rho_\alpha = \rho_\beta$. The exact position of R is uncertain anyhow by about half the interface thickness δ_{int} (while δ_{int} for a droplet of radius 50 [lu] could be around $5 - 10\%$). The inset in Figure 2 shows the pressure profile along a diametric line across the droplet. The jumps seen in the pressure profile at the interfaces are due to the local definition of P in Eq. 13, and can be remedied using the extended pressure tensor given by Sbragaglia and Belardinelli.[71] We observe a clear linear increase in ΔP with $1/R$, where the slope of the line gives the value of surface tension, and an axis cutoff close to the origin, indicating a convincing agreement with the Laplace law, Eq. 15.

$$\Delta P = \frac{\sigma}{R} \qquad (15)$$

Addition of the surfactant

The surfactant component s is now introduced, which is repelled by both liquid components α and β. The values of $G_{\alpha s}$ and $G_{\beta s}$ are chosen such that the repulsive force on the surfactant from both liquids is equal, which is ensured by maintaining $G_{\alpha s}/G_{\beta s} \approx \rho_\beta/\rho_\alpha$. The miscibility of the surfactant in either fluid can be changed by altering this ratio. All simulations in this section are performed in 2-D on a 200×200 periodic lattice, which is a smaller domain facilitating a wide exploration of the parameter space while keeping the computational cost modest. The following results do not depend on the domain size.

The droplet is initialized at the center with a radius of 30 [lu] and the surfactant is uniformly distributed throughout the domain. The liquid–liquid density ratio is chosen to be $\rho_{\alpha\beta}^\star \sim 1.44$ (where $\rho_{\alpha\beta}^\star = \rho_\alpha/\rho_\beta$) while $\rho_{\alpha\beta}^\star$ values from $\mathcal{O}(1)$ to $\mathcal{O}(1000)$ are possible, and the liquid-surfactant density ratio $\rho_{\alpha s}^\star \sim 1000$.

The EOS parameters have been fixed to the values mentioned in Table 2. These values are chosen such that the physical temperature of the system $T = T_c \times T_r$ is constant for all components, while T_r can vary. As we simulate a liquid–liquid system, the values of a and b for components α and β are rather similar. We did not use exactly the same values for both as we let component α undergo internal phase segregation in our modeling approach while maintaining the same temperature for all components. These values should also be considered in relation to those for the surfactant component, where a and b for component s are much larger than for α and β. This is because a larger value of b means a larger internal *hard sphere* like repulsion between surfactant molecules (due to the EOS). This is required to ensure that the surfactant does not form droplets, and in the absence of repulsive forces from components α and β the surfactant remains uniformly distributed. In the presence of repulsion, the surfactant migrates to the interface and redistributes uniformly around it. Here, there is again an optimum, as a very strong internal repulsion (larger b) would result in a very small amount of surfactant to collect at the interface. So the EOS values were chosen by finding an optimal value for b, while a is calculated such that the temperature remains the same as for components α and β. The value of $\beta = 1.25$ in Eq. 10, and all fluid relaxation times τ are set to 1.

Figure 3a shows the steady-state density fields of the three components for a quiescent droplet, where the surfactant is seen to collect at the interface. The normalized density fields $\hat{\rho} = (\rho - \rho_{min})/(\rho_{max} - \rho_{min})$ where $\rho \in \{\rho_\alpha, \rho_\beta, \rho_s\}$ show how the component densities vary across the interface and the surfactant collects between the α and β components. The interface is seen to be roughly 10 [lu] here, which is wider than it is when simulating a *pure* liquid–liquid droplet (~5 [lu]) using the same parameters (i.e., if we set $G_{\alpha s} = G_{\beta s} = 0$). This is due to the surfactant which accumulates between the two fluids and pushes on them. The interface region can in

Table 2. EOS parameters (refer to Eq. 11) for the three components that have been fixed for this parameter study. $G_{\sigma\sigma}$, the intracomponent interaction parameter for each parameter, is set to -1 and $R = 1$ for all components. The physical temperature $T = T_c \times T_r$ is the same for each component, that is, they form an isothermal system

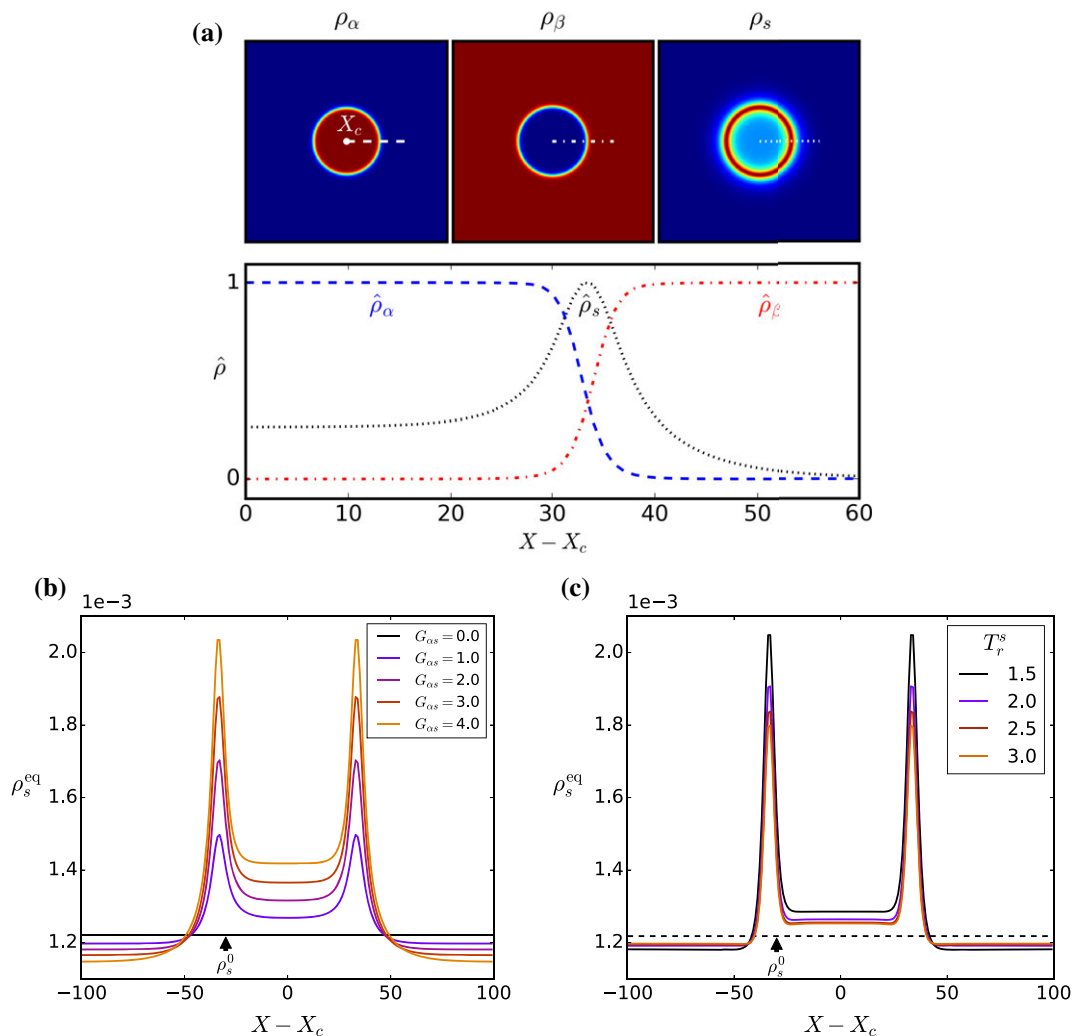| Component	a	b	T_r	T_c
α	0.0068755878	0.18727	0.8	0.01385369
β	0.007343	0.25	1	0.01108295
s	17.62311	600.0	1	0.01108295

Figure 3. Equilibrium component densities from stationary droplet simulations are shown in: Figure 3a as normalized densities in the domain and across the droplet diameter with $\hat{\rho} = (\rho - \rho_{\min})/(\rho_{\max} - \rho_{\min})$ where $\rho \in \{\rho_\alpha, \rho_\beta, \rho_s\}$. Figure 3b shows the surfactant distribution for increasing values of the liquid-surfactant repulsion strength $G_{\alpha s}$ ($G_{\beta s} = 2G_{\alpha s}$ as $\rho^\star_{\alpha\beta} = 2$), where the peak concentration increases with increasing $G_{\alpha s}$ as the surfactant is more strongly repelled by both liquids. Figure 3c shows the same for increasing values of the surfactant reduced temperature T^s_r, where ρ^{eq}_s decreases due to an increased internal surfactant repulsion.

principle be made narrower by changing the surfactant EOS parameters such that it has a lower internal repulsion and a larger amount of surfactant can collect within a small region. It is useful, also with the view of the discussion further on, to conceptually define this ratio of internal surfactant repulsion and external liquid-surfactant repulsion as

$$R_s \sim F_{\mathrm{internal}}/F_{\mathrm{external}} \qquad (16)$$

So the interface width δ_{int} could be proportional to R_s, though R_s cannot assume arbitrarily large or small values. Also note that LB being a diffused interface method, there is a minimum interface thickness (roughly $5-6$ [lu]) below which the droplet becomes unstable and can dissolve away.

Interface widening is an issue faced by all diffuse interface methods. In the multicomponent PP-LB method, a higher repulsion strength between the liquid components ($G_{\alpha\beta}$ in our case), leads to a stronger phase separation and hence sharper interfaces as well as to a higher surface tension. It is difficult

to manipulate these three effects independently. Typically, one would want to have a large enough separation between the droplet radius and the interface width, that is, the ratio $\zeta = R/\delta_{\mathrm{int}}$ should be as large as possible, ideally more than 50 or 100. The diffuse interface in such a case can be expected to have little influence on the results. Such simulations, however, will be very computationally demanding in practice, as one also requires a large enough separation between the droplet radius R and the domain size L. To have both the ratios R/L and ζ high is generally not feasible and one has to compromise the resolution on either or both of these. This is a crucial aspect to be considered when formulating a physical problem to be simulated with any diffuse interface method. With proper scaling of these ratios, the shortcoming of a finite interface width can be overcome to meaningfully simulate the physics. We now use this stationary droplet as a test problem to perform a parameter space investigation of our model. The results presented in this section deal with equilibrium behavior of the model like

interfacial concentrations, surface tension and so forth, which should not be expected to be very sensitive to ζ.

Influence of the Liquid-Surfactant Repulsion Parameter $G_{\alpha s}$. The parameters $G_{\alpha s}$ and $G_{\beta s}$ determine how strongly the components α and β repel the surfactant s. They also determine the extent of immiscibility of s in α and β, and since we keep these values such that s is equally immiscible (or repelled), we discuss this effect in terms of $G_{\alpha s}$ only (while $G_{\beta s} = G_{\alpha s} \times \rho^\star_{\alpha\beta}$). In all simulations, we keep the value of the liquid to surfactant force scaling parameter $S_{\alpha s} \geq 100$ (see Eq. 8) to ensure stability. The equilibrium surfactant concentration across a diametric line through the droplet is shown in Figure 3b for increasing $G_{\alpha s}$.

When starting with the same uniform initial surfactant concentration ρ^0_s, for increasing $G_{\alpha s}$, the equilibrium density of the surfactant at the droplet interface obtains a higher peak. The surfactant concentration outside the droplet falls to a successively lower value showing the conservation of surfactant mass in the system. The final liquid–liquid density ratio $\rho^\star_{\alpha\beta} = 1.42$ while the ratio between the repulsion strengths $G_{\beta s}/G_{\alpha s} = 1.44$. This difference reflects in the surfactant being slightly more miscible in the α component and its concentration inside the droplet increases with $G_{\alpha s}$. For larger repulsion strengths, the interface becomes slightly wider as the surfactant pushes on the two liquids more strongly. It should be noted that for each fluid configuration (i.e., liquid EOS parameters, and density ratio between α, β & s), there is a sensitive upper bound to $G_{\alpha s}$, beyond which the repulsive pseudopotential force becomes too large and simulations are unstable. Here, it is seen that around $G_{\alpha s} \sim 4.5$ the simulations become unstable (with the minimum bounds on the liquid to surfactant force scaling factor being $S_{\alpha s} = 100$ to ensure stability).

We also look into the migration of the surfactant from the bulk towards the interface in Figure 4 for increasing $G_{\alpha s}$, which is done by monitoring the maximum surfactant concentration in the domain (which happens to be at the interface). On increasing $G_{\alpha s}$, at early times the amount of surfactant at the interface increases as the simulation proceeds. However, within around 200 iterations, the maximum concentration for each simulation is attained and the value oscillates around it until equilibrium is attained. This at first seems counter intuitive, as increasing the force acting on the surfactant should result in its faster migration to the interface. Here two things are worth noting, first is that increasing $G_{\alpha s}$ reduces R_s (refer to Eq. 16), and hence a larger amount ρ_s will collect at the interface. Secondly, regarding the rate of migration of ρ_s for a stationary droplet, there is no physical timescale for interpreting the number of iterations for approach to equilibrium, and each iteration simply means a single collision and streaming step. An increasing repulsion force on the surfactant will translate to an increased change in momentum, but since velocities in LB are fixed, this change can only be achieved by streaming a larger density fraction of the surfactant within a time step. Figure 4 is consistent with this reasoning, and all the cases attain their individual maximum surfactant densities after the same number of iterations. Further, the inset shows the density evolution normalized with the final density, and all the cases collapse to a single evolution curve.

A last point to note here is the wiggles in the evolution profile. These are caused by the generation of pressure (sound) waves in the system due to two factors—first the relaxation of the droplet from its initialized profile to an equilibrium profile, and second the sudden addition of the surfactant repulsion
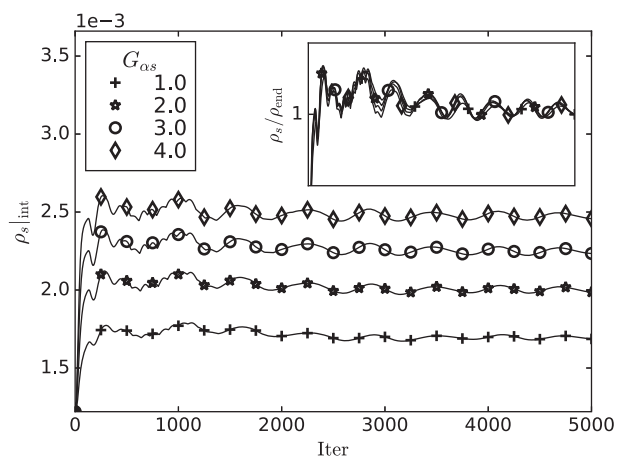

Figure 4. Surfactant migration to the interface increases for increasing repulsion strengths $G_{\alpha s}$, where $S_{\alpha s}$ = 100 and $G_{\alpha\beta}$ = 0.02.

It is seen that the maximum surfactant concentration for each configuration is attained within 200 iterations. The inset shows the normalized density (also from 0 to 5000 Iter), where all cases is seen to follow the same evolution profile.

forces. These wiggles completely disappear after 20,000 iterations, and are present only during the initialization phase. In simulations of incompressible flow, pressure waves are undesirable, and hence these simulations must be performed over a timescale much longer than any initial transient phenomena that may be present, like approach to local equilibrium in LB. Further, it should be ensured that the flow Mach number is reasonably small (where typically $Ma < 0.1$ is desired). Once the initial phase of relaxation to equilibrium is over, any further changes in the component density distributions is due to the hydrodynamics, which proceeds over a longer timescale than the acoustic timescale. Hence our simulations do not suffer from pressure waves.

Influence of the Reduced Temperature T^s_r. Increasing the reduced temperature T^s_r for the surfactant component to values greater than 1.0 increases the internal molecular repulsion within the component, which is similar to the pressure in a gas rising when it is heated as the molecules become more energetic. At higher T^s_r, the force ratio R_s will increase, and the maximum equilibrium density of the surfactant that can collect at the interface will decrease. This is shown in Figure 3c where $G_{\alpha\beta}$ = 0.02, $S_{\alpha s}$ = 100 and $G_{\alpha s}$ = 4.0. To ensure that the surfactant is still at the same temperature as the other two components when $T^s_r > 1$ (i.e., the surfactant is at a supercritical temperature), the EOS parameter a is scaled with $1/T^s_r$ as $T_c = 0.3773322a/Rb$. Note that T^s_r could also be reduced to values lower than 1.0, but that could initiate internal phase segregation within the surfactant component and is not desired.

Indeed, at higher T^s_r the surfactant feels a stronger internal repulsion and R_s increases, consequently a smaller amount of surfactant collects at the interface. This also leads to the interface becoming slightly narrower (as was discussed earlier after Figure 3a) as a lower surfactant density has a lower repulsion strength acting on the two components on either side of the interface.

Influence of the Surfactant Viscosity τ_s. The surfactant viscosity ν_s, which is related to τ_s according to Eq. 6, has been shown to strongly influence the dynamics.[60] The surfactant concentration at a point on the interface is shown in Figure 5
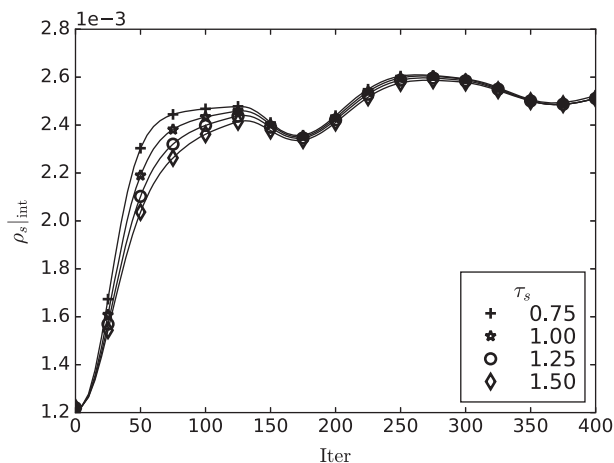
Figure 5. Evolution of the interfacial surfactant concentration $\rho_s|_{\text{int}}$ for varying surfactant relaxation times τ_s (related to the surfactant viscosity ν_s according to Eq. 6). Here, $G_{\alpha\beta} = 0.02$, $G_{\alpha s} = 4.0$, and $S_{\alpha s} = 100$.

for varying τ_s. For the quiescent system studied here, only a slight influence is seen in the approach to equilibrium concentration, where the more viscous surfactant migrates slower. The surfactant viscosity can be expected to influence the dynamics when the characteristic time of the flow is comparable to the diffusion timescale, or for more dynamic problems like falling droplets and so forth. With the current setup, the viscosity ratio between components cannot have very high values, which requires further modifications to the LB method for instance as proposed by Meng and Guo.[72]

Strength of the surfactant

The strength of a real surfactant varies greatly depending on a number of microscopic effects like the extent of ionic dissolution, adsorption of ions at the interface, etc.[21] So far in our modeling approach, the strength of the surfactant depends *only* on the surfactant density (ρ_s) at the interface and how strongly it repels the liquid components, which is given by the repulsion strength parameters $G_{\alpha s}$ and $G_{\beta s}$. While still keeping the discussion in terms of $G_{\alpha s}$ only, we define surfactant strength Λ as

$$\Lambda = G_{\alpha s} \sum_{\text{int}} \rho_s \qquad (17)$$

in which the summation is carried out over the entire interface. Since the interface is diffused, we take this sum within the region bounded by two radii corresponding to the lower and upper bounds on the density of component α, given as $1.1 \times \rho_\alpha^{\min} < \rho_\alpha < 0.99 \times \rho_\alpha^{\max}$. The values 1.1 and 0.99 are somewhat arbitrary, though they accurately capture the interface width, and slightly changing these numbers does not influence the following results. Defining Λ in this way facilitates comparison between simulations even upon varying multiple parameters.

We now investigate the equilibrium surface tension of a stationary droplet in a quiescent periodic domain for increasing surfactant strength. The surface tension is calculated using the Laplace law at steady state where $\Delta P = \sigma/R$, ΔP being the pressure difference (where P is calculated according to Eq. 13) between the center of the droplet and edge of the domain and R is the droplet radius. Figure 6 shows the equilibrium surface

tension over the strength Λ, for two cases of the clean droplet surface tension which was varied by changing the liquid–liquid repulsion strength $G_{\alpha\beta}$. Sets of simulations of varying Λ are performed by varying $0 < G_{\alpha s} < 4.0$ and $100 < S_{\alpha s} < 800$, of which only the $S_{\alpha s} = 100$ cases are shown.

The surface tension reduces with increasing Λ, and the two sets of simulations follow individual σ reduction curves. A maximum σ reduction of around 15% is observed. In our parameter space investigation, we varied the various interaction strengths ($G_{\alpha\beta}$, $G_{\beta s}$, $G_{\alpha s}$), the inner repulsion of the surfactant (which depends on the surfactant EOS parameters a and b, *cf.* Eq. 11), the reduced temperature T_r^s of the surfactant component and the surfactant viscosity ν_s. The results obtained from all these simulations are shown together in Figure 7, where the y axis shows the relative reduction in surface tension σ/σ_0 (where σ_0 is the surface tension of the clean droplet for a particular value of $G_{\alpha\beta}$), and the x axis shows Λ.

A maximum reduction in surface tension of about 15% is achieved, and the largest value of Λ we could simulate with this model is around 25. Higher values of Λ might be possible with suitable extensions to this model which stabilize the system for higher repulsion strengths. Using the multirange interaction method,[71] a different EOS for the components or another collision operator like the MRT[73] could help achieving this, although we have not explored those possibilities in this article. Generally a higher reduction in σ comes at a cost of a wider interface (which goes from roughly 7.5–22.5 [lu]). This is a consequence of a higher concentration of the surfactant repelling the two components at the interface more strongly. The solid black line indicates a Langmuir type of fit of the form

$$\frac{\sigma}{\sigma_0} = 1 + \frac{c}{\sigma_0} RT \log\left(1 - \frac{\Lambda}{\Lambda_{\max}}\right) \qquad (18)$$

where c is a constant fitting factor, and $\Lambda_{\max}$ is taken to be 40 for this fit. The scatter in Figure 7 is due to the use of very different model parameters between cases. Upon varying just one of these parameters while keeping the remaining constant,
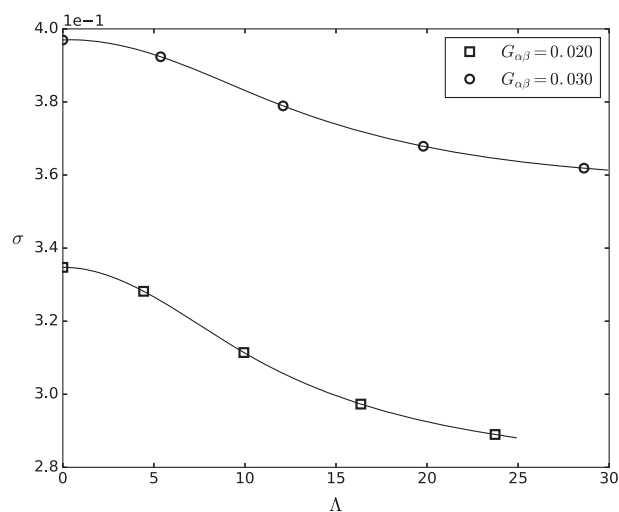

Figure 6. Reduction of the equilibrium surface tension σ for two cases of a clean droplet surface tension which is varied by changing the liquid–liquid repulsion parameter $G_{\alpha\beta}$. Λ is increased by varying $0 < G_{\alpha s} < 4.0$, and $S_{\alpha s} = 100$ for the cases shown.
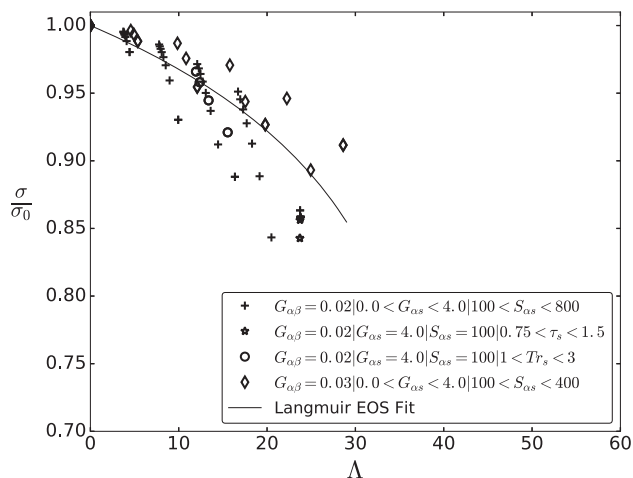
Figure 7. Reduction in the equilibrium surface tension σ/σ_0 for a stationary droplet over the surfactant strength Λ shown for all the cases simulated.

The legend shows the range each parameter was varied over in a simulation set and the solid black line represents a Langmuir EOS fit (refer to Eq. 18). Surface tension reduction seems to be spread around this curve. A larger reduction in surface tension also results in a thickening of the interface.

the pertinent points follow a single curve. Using this model, a few simplified calibration simulations would be required to ascertain the particular isotherm behavior of the parameters under consideration, as surface tension reduction emerges from simplified pseudopotential particle interactions. In alternate techniques like the free-energy method, the desired isotherm is preset into the model thermodynamics, which is in stark contrast to our approach.

In practice, the surfactant layer at a liquid–liquid interface has a thickness of the order of microns, and a reduction in surface tension of 50% or greater is possible. In LB, the interface is diffuse and even at its sharpest, it will be smeared over $5 - 7$ [lu], which also determines the minimum thickness of the surfactant layer, and is also observed in previous work on this problem using the LB method.[43,45,48,49] The interface width here should, however, be valued in comparison to the domain size L, and if $L \gg \delta_{\text{int}}$, theoretically the $5 - 7$ [lu] δ_{int} can be scaled to a small enough physical length scale. This can of course be limiting as larger domains will begin to have prohibitive computational costs, particularly in regards to memory considering a three component system.

Spinodal Decomposition

Moving to a dynamic setting, we investigate the influence of the surfactant on spinodal decomposition,[74] or phase segregation of the two fluid components. To briefly review this phenomenon, consider a single fluid component initialized in a metastable state at a sub critical temperate (or $T_r < 1.0$). Random density fluctuations are added to this component to initiate internal phase segregation where the fluid separates spontaneously into liquid and vapor states with densities determined by its EOS. The fluid initially forms localized droplet-like structures that coalesce and grow over time until the two phases are completely separated. This process, which is rather similar to Ostwald ripening in crystallization, is also denoted by the term "coarsening dynamics."

Additionally, as in our system, a second fluid component may also be present. This second component can also undergo internal phase segregation if it is modeled as a nonideal component by being placed at a sub critical temperature (i.e., $T_r < 1.0$). Or more simply, repulsion from the first component can make the second component collect in liquid-like and vapor-like phases (the liquid and vapor densities here deviate from the Maxwell construction, as these are now formed due to the repulsive interaction with the first component, so that the bulk of the second component exists in regions where the first component exists as vapor). In our work, we model all components as non ideal. The first component, α, is allowed to undergo internal phase segregation by keeping it at $T_r < 1.0$, while the second component β and the surfactant s are kept at $T_r = 1.0$. This ensures that there are no regions in the domain where both components α and β exist in vapor phases, and a truly liquid–liquid configuration is achieved. Distinction between the terms phases and components is crucial, as a single component may exist in two phases, and yet overall the system is liquid–liquid, due to the presence of another liquid component.

Due to phase segregation interfaces emerge, and depending on the initial density of the components, either a symmetric or an asymmetric composition is achieved, the latter of which may result in nucleation or droplet phase separation based upon the initial density distribution.[75] Many studies[76-80] have reported scaling laws that give the temporal evolution of the characteristic domain length of the fluid regions growing due to coalescence over short and long times, for different binary fluid mixtures in both two and three dimensional systems. The addition of surfactants is expected to inhibit the growth rate of this characteristic domain length, which was also observed by Nekovee et al.[43]

To quantify spinodal decomposition, a commonly studied parameter is the structure factor $\hat{S}(\mathbf{k}, t)$ which is obtained by performing a Fourier transform on the instantaneous density correlation function $q(\mathbf{x}, t)$, and contains information of the evolution of various length scales in the system.[42] It is calculated as

$$\hat{S}(\mathbf{k}, t) = \frac{1}{N} \left(\sum_{\mathbf{x}} [q(\mathbf{x}, t) - \overline{q}(t)] e^{i\mathbf{k} \cdot \mathbf{x}} \right)^2 \qquad (19)$$

where $q(\mathbf{x}, t) = \rho_\alpha(\mathbf{x}, t) - \rho_\beta(\mathbf{x}, t)$ denotes the density difference between the two components at location $\mathbf{x}$ at time t, $\overline{q}(t)$ is the spatial average of q at each time step and N is the number of grid points (i.e. $N_x \times N_y$). Here $\mathbf{k}$ is a 2-D wavenumber, as the Fourier transform yields a 2-D matrix of values. To convert this to a single spatial wavenumber k, the structure factor is averaged over shells in $\mathbf{k}$ space to yield the spherically averaged quantity $\hat{S}(k, t)$ as

$$\hat{S}(k, t) = \frac{\sum_{\mathbf{k}} \hat{S}(\mathbf{k}, t)}{N_{\mathbf{k}}} \qquad (20)$$

where the sum $\sum_{\mathbf{k}}$ is over circular shells defined by $\mathbf{k} = \sqrt{k_x^2 + k_y^2}$, and $N_{\mathbf{k}}$ is the number of all k_x and k_y pairs corresponding to each $\mathbf{k}$ shell.[42] The wavenumber corresponding to any length $\mathscr{L}$ is defined as $k = 2\pi/\mathscr{L}$. Considering the domain length to be N_x [lu] in each direction, the smallest non-zero wavenumber (largest scale) is $k_{\min} = 2\pi/N_x$, while the largest wavenumber (smallest scale) is given by $k_{\max} = 2\pi/2 = \pi$ (which is similar to a Nyquist frequency). Further, the

domain growth represented by the characteristic length $R(t)$ can be calculated using the first moment of $\hat{S}(k,t)$ as

$$R(t) = 2\pi \left(\frac{\sum_k \hat{S}(k,t)}{\sum_k k\hat{S}(k,t)} \right) \qquad (21)$$

For asymmetric phase fractions of the two fluids, $R(t)$ is expected to follow a $t^{1/3}$ power law[79,81] in the inertial regime where capillary forces are minor.

In our simulations, all three components are initialized with a uniform density field, where the density ratios are $\rho^\star_{\alpha\beta} \sim 1.44$ and $\rho^\star_{\alpha s} \sim 10^3$, $G_{\alpha\beta} = 0.02$ and $S_{\alpha s} = 100$. The denser component α is at a reduced temperature $T^\alpha_r = 0.8$ and random density fluctuations (with zero mean) are added to initiate internal phase segregation, the lighter fluid and surfactant both are kept at $T^\beta_r = T^s_r = 1$. The domain size is 512×512 [lu]. The evolution of the α component and the surfactant is shown in Figure 8, for the case with $G_{\alpha s} = 4.0$. It is seen that small localized regions of the heavy component form within a short time which then coalesce and grow, while the surfactant adheres to the evolving interfaces.

Next, the structure factor $\hat{S}(k,t)$ is presented as a spectral density map in Figure 9 for $G_{\alpha s}$ = 0.0, 2.0, 4.0 from top to bottom. Here, $\hat{S}(k,t)$ has been further normalized by the maximum value at each time step to highlight the relative growth of different scales over time.

Two distinct evolution regimes can be seen, first being a region of fast growth where within 1500 iterations small scale structures are formed and there are several contributing length scales to $\hat{S}(k,t)$, which evolve from around $k\sim0.25$ to $k\sim0.12$. From iteration 1500 to 10,000, a second regime of slow dynamics is observed and the system proceeds towards a dominant length scale (as is seen from the spectral density showing strongly concentrated modes, as the spread over k becomes narrower). Over longer times, it is seen that the dominant wavenumbers are more or less similar for the clean and surfactant laden cases ($k\sim0.05 - 0.025$), with only slight variation in the evolution profiles.

At steady state, we observe that the volume fractions of component α and β are 0.4 and 0.6 approximately, showing that our initial conditions lead to an asymmetric composition. The situation obtained is that of liquid droplets of the heavier fluid forming the dispersed phase while the lighter fluid forms the continuous medium. On changing the initial densities, the reverse was also observed but this has been excluded from this article.

Lastly, the evolution of the characteristic length $R(t)$ has been shown in Figure 10 for cases with increasing $G_{\alpha s}$. No change in the expected $t^{1/3}$ exponent is found for increasing surfactant strength. Even though the highest surfactant strength reduces surface tension by 15% for a stationary droplet, this has little influence on the coalescence behavior in a dynamic setting. This is not entirely surprising, as currently our surfactant model does not contain a mechanism for explicitly shielding coalescence, which we shall shortly discuss.

One of the benefits of the LB method and our modeling approach is the ease of extension to 3-D, with efficient parallelization. We extend our multicomponent approach to a D3Q19 lattice to simulate spinodal decomposition in a 256^3 3-D periodic domain. The same parameters as in the 2-D case are taken. Figure 11 shows the density evolution of component α as the white contours in the column a, along with the surfactant density field thresholded at 75% of the maximum value in

ρ/ρ^{max}

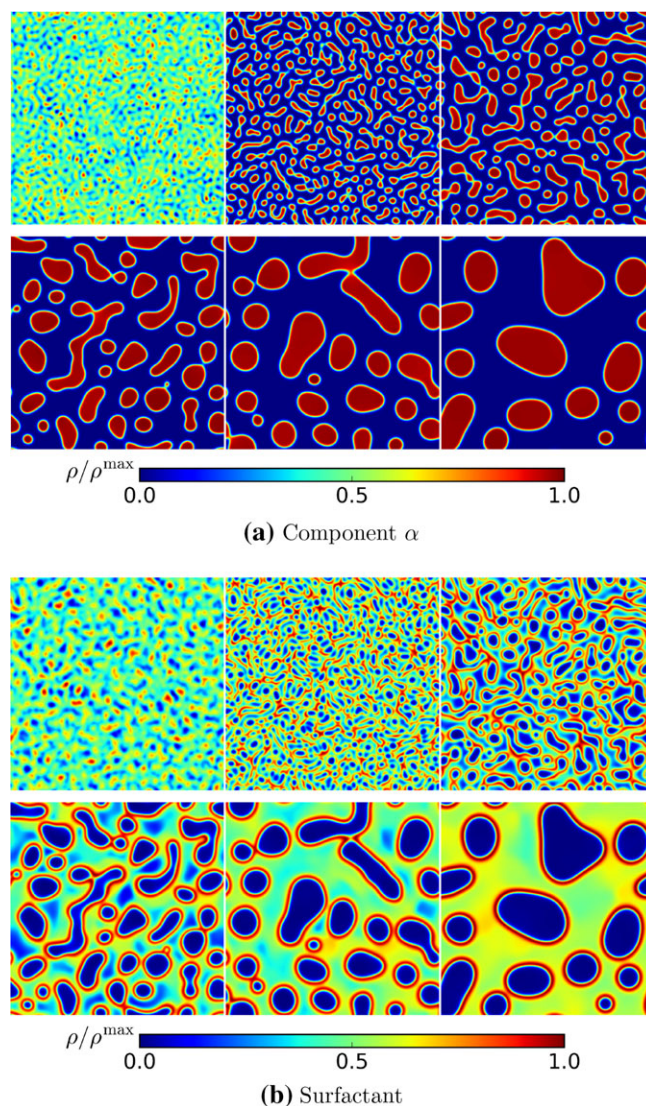0.0   0.5   1.0

(b) Surfactant

Figure 8. Normalized density field of component α and surfactant s (with blue to red representing minimum to maximum value) at Iterations 100, 500, 1000, 2500, 5000, and 10,000 for phase segregation, with $G_{\alpha\beta}$ = 0.02 and $G_{\alpha s}$ = 4.0. The final volume fractions of α and β are 0.4 and 0.6.

column b. These results correspond to the $G_{\alpha s}$ = 2.0 case, while $G_{\alpha\beta} = 0.04$. The rows correspond to iterations 600, 1000, and 2000 from top to bottom. The surfactant adapts very well to the three dimensional evolving interfaces, in a decaying quasiturbulent field which is generated by the conversion of the large initial surface energy (driven by interfacial tension) to kinetic energy (on droplet coalescence). It is worthwhile to note the computational cost of such a simulation. The domain consists of more than 16 million lattice nodes, and the three component modeling approach with 19 velocity directions in 3-D requires one to store 19×3 density distribution values (f^σ_i) at each lattice unit which in double precision amounts to around 8 GB of memory. Simulating 10,000 iterations took approximately 10 h of wall-clock time on 24 processors. A further resolution doubling would make the memory requirements eight times and computation time 16 times larger, soon becoming prohibitively expensive.
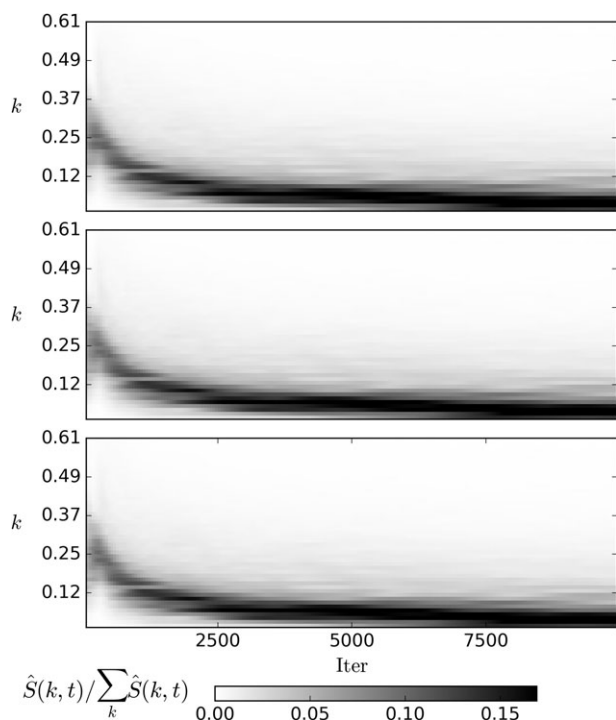
Figure 9. Spectral density map of the spherically averaged structure function $\hat{S}(k,t)$ (normalized by the total spectral density at each timestep $\sum_k \hat{S}(k,t)$), with the spatial wavenumber k on the y axis (showing only the first 50 values out of the total 256), and the iteration number on the x axis which goes from 1 to 10,000.

The cases shown from top to bottom correspond to $G_{\alpha s}$ = 0.0, 2.0 and 4.0. Initially the distribution peaks around $k{\sim}0.25$, that it, small dispersed droplets which then grow rapidly up to iteration 1500 to $k{\sim}0.12$, after which the evolution is slow. We do not observe any influence of the surfactant on the evolution of $\hat{S}(k,t)$.

Figure 11 column c shows composite density fields, with contours of component α over half the domain and the surfactant density thresholded at 75% of the maximum value at iteration 1000, for $G_{\alpha s}$ = 2.0 (above) and $G_{\alpha s}$ = 4.0 (below). Some qualitative difference can be seen between the two figures, particularly that the local concentrations of the surfactant are higher (a larger predominance of yellow–green regions). The α contours, however, are rather similar between the two cases.

Coalescence inhibition

Previous research on surfactant laden emulsions has included an additional aspect capable of abetting inhibition of coalescence. Chen et al.,[42] Furtado and Skartlien,[45] and Skartlien et al.[44] consider a dipole orientation of the surfactant that responds to a mean field generated by surrounding dipole distributions. This might make it energetically favorable for dipoles to orient in certain manners that prevent droplet coalescence. In addition, a long range intracomponent repulsive interaction force, in addition to the short range attraction has been demonstrated to shield droplets in approach from coalescing *without* the need of a surfactant component.[47,82,83] However, such a method does not truly represent surfactant dynamics, as it cannot give rise to Marangoni effects or modify interfacial boundary conditions.

As was seen from the spinodal decomposition studies, increasing surfactant strength did not prevent coalescence of droplets in our model. This is because despite the accumulation of the surfactant at the interface, there is no mechanism for preventing coalescence from taking place, the components α and β still repel each other to the same degree as in the absence of the surfactant, such that the resulting film drainage between approaching droplets still causes them to coalesce. Following this reasoning, we propose an extension of the current model, that is, to make $G_{\alpha\beta}$ a function of the local surfactant density. When the surfactant now collects at the interface, it can alter how strongly α repels β, in turn influencing the drainage of component β when two droplets of α approach each other.

We implement this in our model as

$$G_{\alpha\beta} = G_{\alpha\beta}^0 \left(1 - c \left[\frac{\rho_s}{\rho_s^{\max}}\right]^p\right) \qquad (22)$$

where $G_{\alpha\beta}$ now varies over the domain, $G_{\alpha\beta}^0$ is the maximum repulsion value (corresponding to the case when no surfactant is present), ρ_s is the surfactant density at a local lattice node which is normalized by the instantaneous maximum surfactant density anywhere in the domain $\rho_s^{\max}$. Alternatively, the surfactant density could also be normalized by a prefixed value that is large enough to yield a fraction between 0 and 1, though if the chosen value is too large, the dynamics would not be significantly altered, which we observed in some unreported simulations. The exponent $p = 1$ creates a linear variation in the $G_{\alpha\beta}$ profile, which might not be optimal, as immiscibility between α and β is desired to reduce more rapidly when ρ_s approaches $\rho_s^{\max}$ than when ρ_s assumes smaller values. We set $p = 3$ after some preliminary testing. Further, c sets the minimum bounds on the reduction in $G_{\alpha\beta}$, and a few values were tested, whereafter, we set it to $c = 0.5$. A similar treatment is done to $G_{\alpha\alpha}$ with $p = 3$ and $c = 0.1$, so as not to drastically alter the intracomponent attraction in α to an extent that droplets of α begin to dissolve away. To demonstrate the influence of this technique, we redo the 2-D spinodal decomposition cases presented earlier on a 512×512 domain, with $G_{\alpha s}$ = 2.0, and the evolution of $R(t)$ is shown in Figure 12.

The cases with varying $G_{\alpha\beta}$ and $G_{\alpha\alpha}$ show a flattening of $R(t)$ at a lower value within 5000 iterations with a clear
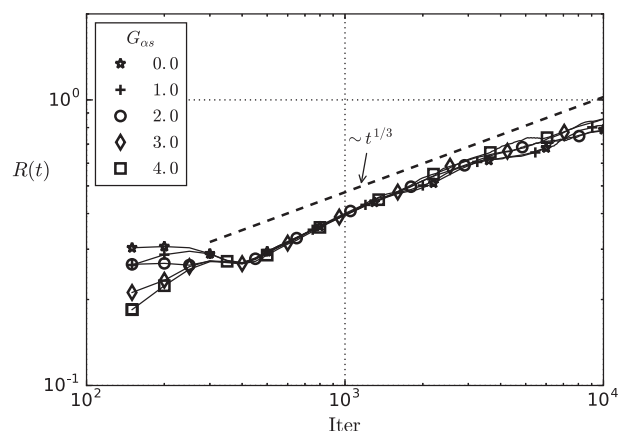

Figure 10. Growth of the characteristic length scale $R(t)$ for increasing $G_{\alpha s}$ is shown.

No influence of an increasing surfactant strength is observed on the growth rate of $R(t)$, which follows a roughly $t^{1/3}$ scaling as reported in literature.[79,81]
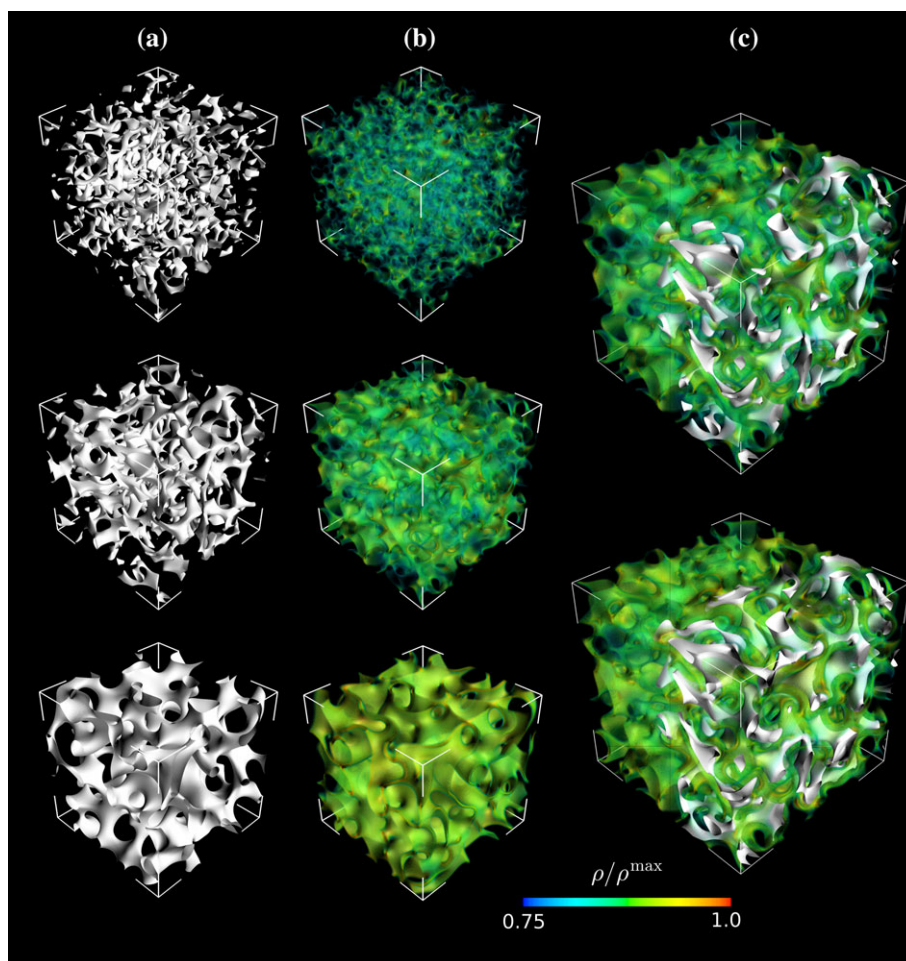
Figure 11. Spinodal decomposition in three dimensions is shown, with the contours of component α in column *a* and surfactant density thresholded at 75% of the maximum value in column *b*. The three rows correspond to iterations 600, 1000, and 2000. The third column, *c*, shows composite density fields: the bulk surfactant density (again thresholded at 75% of the maximum value) in the entire domain along with contours of component α (in white) in only half of the domain—all at iteration 1000. The value of $G_{\alpha s}$ = 2.0 (above) and $G_{\alpha s}$ = 4.0 (below).

deviation from the $t^{1/3}$ scaling, as compared to the case with constant parameters. This shows that inhibition of coalescence can be achieved, though it should be noted that varying $G_{\alpha\beta}$ and $G_{\alpha\alpha}$ also influences the surfactant density through the intercomponent interactions - the dynamics is hence rather complicated. It was observed (not included in this paper) that using larger values of c (for instance $c = 2$) can result in a change in the sign of $G_{\alpha\beta}$, whereby droplets of α can spontaneouly rip apart into smaller droplets. The growth of $R(t)$ in such simulations is also arrested in a similar way as for the case shown in Figure 12. These simulations did not exhibit an approach to steady state, and the spontaneous generation of small droplets is qualitatively similar to the formation of microemulsions. Also with this modification, the force scaling factor in Eq. 8 is not required. The surfactant density, despite being low and interacting weakly with the other components, is sufficient information as a scalar field that is used to influence other model parameters governing miscibility. This would ensure momentum conservation in nonperiodic domains as well.

Droplet Formation

Finally, we apply our model to a well known multiphase flow problem, the formation of a pendent droplet, a phenomenon ubiquitous in nature and many industrial processes. It involves the formation of a droplet at an aperture driven by a pressure difference (here due to the action of gravity), whereby the droplet grows under the pull of its own weight,
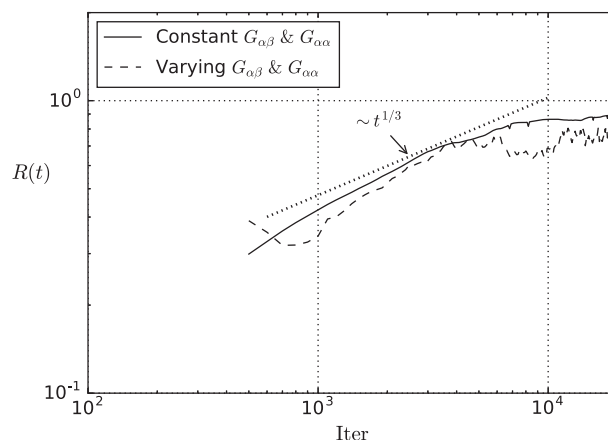

Figure 12. Growth of the characteristic length scale $R(t)$ for two cases of variable and constant $G_{\alpha\beta}$ and $G_{\alpha\alpha}$ values is shown.

The case with varying parameters shows a clear deviation from the $t^{1/3}$ scaling, with $R(t)$ flattening at a lower value within 5000 iterations.

eventually pinching off and falling away—reminiscent of a leaky faucet. This is a complex dynamical process, the crucial moment being the pinch-off, when the droplet breaks away from the reservoir fluid jet, and the process repeats until the reservoir is depleted. We simulate this for clean and surfactant laden cases, mainly focused on illustrating how the surfactant dynamics is captured by our model. Note that we do not investigate the physics here in detail—which can form a study of its own, and use this section as a preliminary demonstration.

We simulate this problem in 2-D, where a pocket of a high density fluid consisting of component α in its liquid phase is initialized above an aperture. The surrounding domain is occupied by a lower density fluid β, also in its liquid phase. The density ratio between the components is $\rho^{\star}_{\alpha\beta} \sim 1.4$, while $\rho^{\star}_{\alpha\beta}$ up to $\mathcal{O}(100)$ is possible. The surfactant component is initialized uniformly throughout the entire domain, with $\rho^{\star}_{\alpha s} \sim 1000$. All components are nonideal and modeled by means of the CS EOS, the relevant EOS parameters being presented in Table 3. Because we simulate three components, we are increasingly restricted by memory limitations, and to keep computational cost modest the size of the domain is kept to $N_x \times N_y = 400 \times 900$ [lu], with the aperture placed at a height of 600 [lu] at the center of the horizontal axis, and has a size of 30 [lu] $\times$ 40 [lu] (width $\times$ height).

Once the system achieves equilibrium in a stationary configuration, a gravitational force is applied to components α and β as $\mathbf{F} = \mathbf{g}\rho_{\sigma}$ with $|\mathbf{g}| = 6 \times 10^{-6}$ [lu] to initiate droplet formation in the dripping regime in the absence of an imposed velocity. This strategy resembles the production of droplets by a push-mode piezoelectric Droplet-on-Demand ink jet print head. Dong et al.[84] describe such a drop formation process in terms of three stages: a first stage, in which the droplet gradually grows while pending, followed by a second stage of stretching and necking, after which the droplet is released and the elongated neck contracts and forms the start of a new droplet. The domain is periodic in all directions, which ensures a continuous production of droplets, and the simulations are run for 2 million iterations, while collecting droplet statistics every 200 iterations. These simulations take roughly 48 h of wall-clock time when run in parallel on 15 processors.

The cases simulated are presented in Table 4. For the "Clean" case DF1, there is no interaction between the surfactant component and the two liquid components, such that this is effectively a two component system. For the *surfactant-laden* cases, we turn on interaction between the surfactant and the fluid components, the strengths of which are presented in Table 4. The cases DF2 and DF3 are formulated such that the surfactant is slightly more soluble in component α and β, respectively. This is to first demonstrate how such a miscibility can be achieved, as it is often found in real systems. Second, this alters the modification of surface tension by changing the pressure drop across the droplet interface, due to

Table 3. EOS parameters used for the droplet formation simulations. Here, ρ_l and ρ_v represent the component densities in the individual liquid and vapor phases, respectively, and are values used to initialize the simulation

	α	β	s
a	0.006875	0.0073429	17.623
b	0.18727	0.25	600.0
T_r	0.8	1	1
ρ_l	7.7	5.3	0.002
ρ_v	0.05	0.05	0.002

Table 4. Interaction strengths for the various cases

	DF1	DF2	DF3
$G_{\alpha\beta}$	0.0085	0.0085	0.0085
$G_{\alpha s}$	0.0	4.2	4.0
$G_{\beta s}$	0.0	7.5	5.6
$S_{\alpha s}$	–	100.0	100.0

the presence of the surfactant. To the best of the authors' knowledge, this is also the first study to simulate the formation of a droplet for a multicomponent multiphase system with non-ideal fluids and a non-unity density ratio.

Figure 13 shows the droplet formation process, with component α (in red) suspended in component β (in blue), for the clean case (DF1) in the top row. We observe the formation of a stretching neck that pinches off droplets which eventually fall off. The periodic boundaries of our domain in the direction of the body force causes the exiting droplets to re-enter the domain above the aperture (not shown here) and merge with the heavy fluid reservoir. The middle panel shows the same for case DF2, while the bottom panel shows the surfactant density field normalized with the maximum value for DF2.

Several features here are worth noting. Qualitatively, we can see that at iteration 18,000 while the droplet is still attached to the jet for the Clean case, for the DF2 case the droplet already breaks off, which may be attributed to the reduced surface tension in DF2. Further, in the surfactant density evolution, vacuous blue regions with very little surfactant density are formed when the droplet breaks off, forming temporary surfactant *depletion* regions. Transport from the bulk and the internal surfactant repulsion replenishes these regions over time. Also, the surfactant density is higher at the trailing edge of the droplet interface, as the surfactant is swept backwards by the flow.

Around 1200 droplet formation instances have been identified during the entire simulation, which are then used to calculate the probability distribution of the equivalent droplet radii R_{eq} (found by equating the droplet area to a circle with equal area), droplet major axis L, duration between successive droplet formation instances ΔIt and the droplet center of mass position in the lateral direction X_{cm} (which shows how much the droplet oscillates from the central vertical line, where it was produced). The PDFs of these quantities are shown in the first four panels of Figure 14. The PDF of r_{eq} shows that the clean case (black curve) has a strong peak at $R_{\mathrm{eq}} = 29$. The DF2 case does not drastically alter the PDF, though the peak shifts to around $R_{\mathrm{eq}} = 32$ which could be due to a slight thickening of the interface with the presence of the surfactant (as was also encountered in previous sections). For DF3, where the surfactant is slightly more soluble in the surrounding fluid, the peak drops significantly, and a larger number of droplets with $R_{\mathrm{eq}} < 30$ are formed. This trend is similar for the droplet major axis L, which is the lateral extent of the droplet when it is not perfectly circular. Note that with the interface width being around 6–7 [lu], statistics below $R_{\mathrm{eq}} = 15$ and $L = 15$ would not be meaningful.

The PDF of the interval between droplet formation shows a few interesting features of the dynamics governing the problem. For the clean case, a strong peak is seen around ΔIt $\approx$ 3500, and a slightly smaller peak around ΔIt $\approx$ 1750. The first one corresponds to a primary droplet break-off event, following which the depleted fluid jet retracts slightly towards the aperture due to surface tension, and it slowly begins to grow again as more fluid flows through the aperture. After
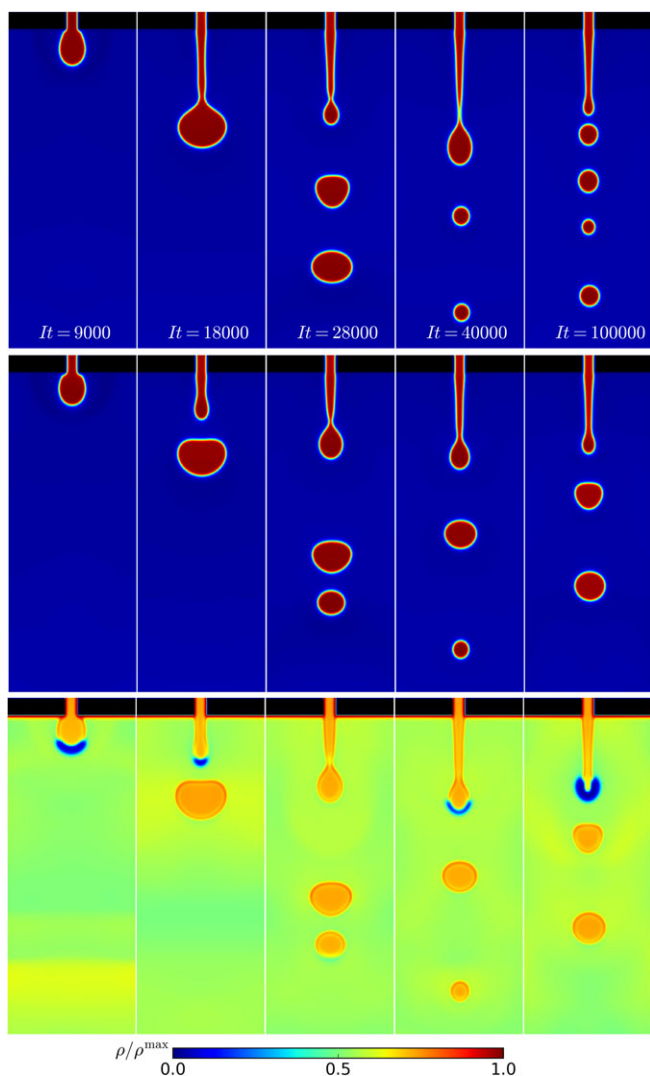
Figure 13. Density fields from droplet formation simulations at various time steps show the liquid α in red (β in blue) for a clean case (top row), liquid α for a surfactant laden case (middle row) and the surfactant density s (bottom row).

The black bands represent the aperture. It can be seen that the surfactant laden case accelerates droplet breakup in the initial period (due to a reduction in surface tension). The surfactant is seen to closely follow the evolving interfaces, with a higher concentration at the trailing edge of the droplet.

some of the droplet pinch-off events following this dominant mode, there is a secondary pinch-off of a smaller droplet, which is also reflected in the PDF of R_{eq}. For the DF3 case, the PDF appears flattened as droplet formation becomes more irregular due to the intermittent presence of the surfactant (as seen in Figure 13), resulting in the smaller droplets pinching off over a shorter timescale, and larger droplets taking longer to do so.

The PDF of $X_{cm} - X_0$ normalized by the domain width W, (with X_0 the center of the domain in the horizontal direction), is very similar for all three cases, with some qualitative differences. Generally, we expect droplets to fall along the central axis without oscillations in the lateral direction as there is perfect symmetry across the central axis. This is true for the initial stages of the simulation (upto the formation of

$\approx$150 droplets and $t < 200000\ \Delta t$). As we use vertical periodicity to ensure a continuous and steady supply of the droplet fluid, the droplets coalesce with the small reservoir above the aperture after re-entering the domain. This in turn generates some long wavelength oscillations in the free surface, which are sustained due to frequent droplet coalescence. The vertical extent of the reservoir is not sufficiently large to completely damp these perturbations out and they later begin to weakly interact with the fluid jet at the aperture. As these free surface oscillations are not perfectly symmetrical across the central axis at longer times $t > 200000\ \Delta t$ (where even machine level inaccuracies might amplify over time due to the inherent non-linearity of the process), the liquid jet begins to swing with a low frequency and low amplitude oscillation which causes a slight spread in the center of mass location of the newly formed droplets. This could be remedied by having a much larger reservoir above the aperture, and the behavior may be less prominent at higher density ratios where the gravitational pull will dominate any lateral lift forces. Notwithstanding, this effect is minor in our simulations, and even the maximum lateral shift ($\approx$9% of W) is slightly larger than the aperture width, that is, 7.5% of W.

A critical Capillary and Reynolds number can be ascribed to the droplet just after pinch off as

$$Re_{cr} = \frac{\rho v L}{\mu}$$

$$Ca_{cr} = \frac{\mu v}{\sigma} \qquad (23)$$

where L is the lateral droplet extent, σ is the surface tension, and ρ and μ are the density and dynamic viscosity of component β (the surrounding fluid). Here, v is taken to be the characteristic droplet velocity calculated as the mean vertical velocity inside the droplet as

$$v = \frac{\sum\limits_{i=1}^{N} v_i}{N} \qquad (24)$$

where i goes over all the N points comprising the interior of the droplet region. From the Figure 14, it was seen that in case DF3, the droplet characteristics change more significantly as compared to the clean case. We show the PDFs of the critical Re and Ca numbers for the clean and DF3 case in the last two panels of Figure 14. The surfactant significantly alters Re_{cr}, and the distribution shifts to a wider range of lower Re_{cr} values, between 6 and 10 for the DF3 case. The surfactant also shifts the peak of the Ca_{cr} PDF from a value of $Ca_{cr} \approx 0.4$ to $Ca_{cr} \approx 0.2$. The presence of the surfactant reduces surface tension, but also causes the formation of smaller droplets which typically have a lower fall velocity. These changes together influence Ca_{cr}, which is found to reduce here. If μ and v are kept constant, surfactant induced surface tension reduction would increase Ca. Controlling these effects individually, however, requires much more precise problem formulation and further investigation. In future work, we intend to test the model for realistic flow problems, along with validation and comparison to existing literature—which was not yet done during this developmental period and parameter space investigation we present in this article, as that can comprise a work unto itself.
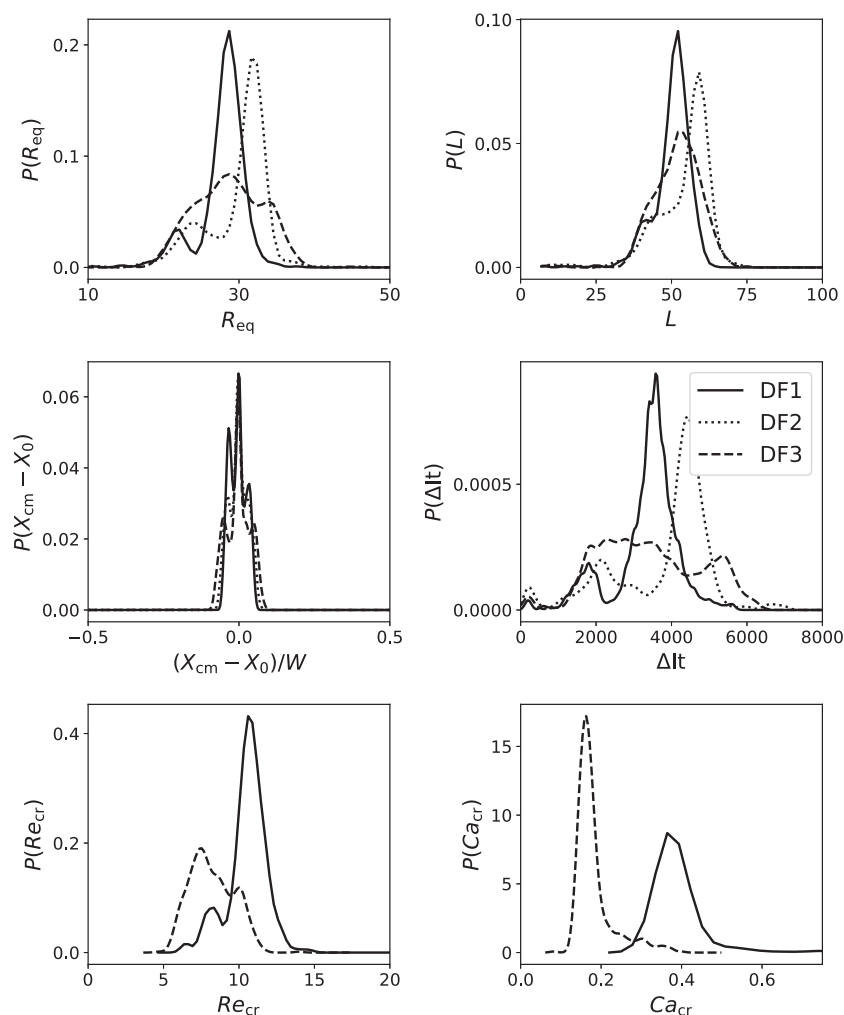
Figure 14. Probability distribution of the droplet equivalent radius $P(r_{eq})$, droplet major axis length L, duration between successive droplet formation events ΔIt and the droplet center of mass in the lateral direction X_{cm} is shown for the clean (DF1) and two surfactant laden (DF2, DF3) cases for the droplet formation problem in the first four panels. The bottom two panels show the critical Reynolds and Capillary number just after droplet pinch-off for DF1 and DF3, where the presence of the surfactant is seen to significantly alter the dynamics.

Conclusions

We have presented a pseudopotential lattice-Boltzmann method to simulate liquid–liquid emulsions with a slightly soluble surfactant component. This is a step towards simulating realistic fluid mixtures which are inevitably surfactant laden, while numerical simulations of multiphase flows have traditionally dealt with pure fluids owing to the complexity involved in simulating surfactant dynamics while resolving fluid motion. The novelty of our work is that we use a simplified model for the surfactant in comparison to previous papers. More specifically, our approach is a simplification of the Chen et al.,[42] Nekovee et al.[43] model, as we ignored orientational effects of the surfactant—an assumption we allowed ourselves to make as we did not intend to study complex aggregate behavior attributed to dipole dynamics. We think that a simplification is also welcome as the original model is quite complex—and has hence not found widespread application. Further, we wish to see how well a simplified model compares to existing methods and what kind of physics it can simulate.

First, a single component pseudopotential LB model was validated for a non-ideal fluid component against the Maxwell reconstruction of coexisting phases. After adding a second fluid component to the system, the model was validated

against the Laplace law for surface tension of a stationary droplet. While simplifying the model for the surfactant, we indeed used a slightly more complicated model for the fluids. Using nonideal equations of state to model the fluids is a continuation of our previous work where we intend to simulate realistic fluids. Additionally, this method allows for simulating flows with a wide range of density ratios, which is not feasible with the classic Shan-Chen based models, and neither has it been reported in other work cited in this paper.

Thereafter, a third surfactant component was added to the system in such a way that it is repelled by the two fluid components, hence aggregating at the interfaces. A parameter study was performed on a stationary, surfactant laden droplet in 2-D to demonstrate the influence of varying the model parameters like the various repulsion strengths, the surfactant viscosity, EOS parameters and the reduced temperature of the surfactant. On defining a surfactant strength parameter Λ, surface tension reductions with respect to a clean interface up to 15% were found to vary with Λ according to, roughly, a Langmuir type of isotherm. To the best of our knowledge, we are the first to demonstrate surface tension reduction for a surfactant laden droplet following Langmuir-like kinetics from purely pseudopotential particle interactions. All other models

addressing this problem work with preset thermodynamics (where an isotherm is fixed), whereby in our approach this emerges from more fundamental interactions.

This simplistic surfactant model, despite the surface tension reduction, was found incapable of arresting phase segregation in 2-D and 3-D spinodal decomposition, achieving which requires an additional mechanism. We proposed varying the liquid–liquid repulsion parameter depending on the local surfactant density, which achieved this effect to some extent. Additional mechanisms like longer-range interaction forces have also been proposed in existing literature to achieve a similar effect. We also performed 3-D spinodal decomposition, where the surfactant was shown to closely follow the dynamic, complex interfaces, making the model viable for future applications to more realistic droplet laden systems in 3-D.

Finally, the model was demonstrated for a well-known physical problem—the formation of a pendant droplet in a liquid–liquid system for both clean and surfactant laden cases, in 2-D. The density ratio simulated was $\rho^\star \approx 1.4$, as we focus on emulsion-like systems. The surfactant was capable of greatly altering the droplet distribution, abetting the formation of more numerous smaller droplets, which we ascribe to the reduced surface tension in the surfactant laden system. The critical Capillary and Reynolds number distributions were also significantly altered. We have also found local differences in the surfactant density between the nose and rear side of pendant and falling droplets.

Our model could also be applied to simulate liquid–gas systems in the presence of a surfactant, and is one of the first studies to simulate three nonideal fluid components. In future work, we shall investigate the currently observed surfactant effects more closely to see whether the model can simulate Marangoni flows, which remains to be ascertained. Further, we intend to more quantitatively compare our model to flow problems, like shear induced breakup of surfactant laden droplets and droplets in turbulent flows.

Acknowledgments

Literature Cited

1. Schaller RR. Moore's law: past, present and future. *IEEE Spectr.* 1997;34(6):52-59.
2. Patankar SV, Spalding DB. A calculation procedure for heat, mass and momentum transfer in three-dimensional parabolic flows. *Int J Heat Mass Transf.* 1972;15(10):1787-1806.
3. Eggels JG. Direct and large-eddy simulation of turbulent fluid flow using the lattice-boltzmann scheme. *Int J Heat Fluid Flow.* 1996; 17(3):307-323.
4. Derksen J, Van den Akker H. Parallel simulation of turbulent fluid flow in a mixing tank. In: Sloot P, Bubak M, Hertzberger B, editors. *High-Performance Computing and Networking.* HPCN-Europe 1998. Lecture Notes in Computer Science, vol 1401. Berlin, Heidelberg: Springer, 1998:96-104.
5. Derksen J, Van Den Akker HEA. Large eddy simulations on the flow driven by a rushton turbine. *AIChE J.* 1999;45(2):209-221.
6. Van Wageningen W, Kandhai D, Mudde R, Van Den Akker HEA. Dynamic flow in a kenics static mixer: an assessment of various cfd methods. *AIChE J.* 2004;50(8):1684-1696.
7. Gillissen J, Van den Akker HEA. Direct numerical simulation of the turbulent flow in a baffled tank driven by a rushton turbine. *AIChE J.* 2012;58(12):3878-3890.
8. Ten Cate A, Derksen JJ, Portela LM, Van Den Akker HEA. Fully resolved simulations of colliding monodisperse spheres in forced iso-tropic turbulence. *J Fluid Mech.* 2004;519:233-271.
9. Derksen J, Van Den Akker HEA. Multi-scale simulations of stirred liquid–liquid dispersions. *Chem Eng Res Des.* 2007;85(5):697-702.
10. Rothman DH, Zaleski S. Lattice-gas models of phase separation: interfaces, phase transitions, and multiphase flow. *Rev Mod Phys.* 1994; 66(4):1417-1479.
11. Scardovelli R, Zaleski S. Direct numerical simulation of free-surface and interfacial flow. *Annu Rev Fluid Mech.* 1999;31(1):567-603.
12. Mukherjee S, Zarghami A, Haringa C, van As K, Kenjeres S, Van den Akker HEA. Simulating liquid droplets: a quantitative assessment of lattice boltzmann and volume of fluid methods. *Int J Heat Fluid Flow.* 2017;70:59-78.
13. Ladd A, Verberg R. Lattice-boltzmann simulations of particle-fluid suspensions. *J Stat Phys.* 2001;104(5–6):1191-1251.
14. Van der Sman R. Simulations of confined suspension flow at multiple length scales. *Soft Matter.* 2009;5(22):4376-4387.
15. Deen N, Kuipers J. Direct numerical simulation (dns) of mass, momentum and heat transfer in dense fluid-particle systems. *Curr Opin Chem Eng.* 2014;5:84-89.
16. Ladd AJ. Lattice-boltzmann methods for suspensions of solid particles. *Mol Phys.* 2015;113(17–18):2531-2537.
17. Ramkrishna D. *Population balances: Theory and applications to particulate systems in engineering.* United States of America: Academic press; 2000.
18. Layrisse I, Rivas H, Intevep S, Acevedo S. Isolation and characterization of natural surfactants present in extra heavy crude oils. *J Dispers Sci Technol.* 1984;5(1):1-18.
19. Banat IM. Biosurfactants production and possible uses in microbial enhanced oil recovery and oil pollution remediation: a review. *Bioresour Technol.* 1995;51(1):1-12.
20. Kokal, S. Crude oil emulsions: A state-of-the-art review. In: *SPE Annual Technical Conference and Exhibition,* San Antonio: Society of Petroleum Engineers, 2002.
21. Rosen MJ, Kunjappu JT. *Surfactants and interfacial phenomena.* New York: Wiley; 2012.
22. Stone H, Leal L. The effects of surfactants on drop deformation and breakup. *J Fluid Mech.* 1990;220:161-186.
23. Eggleton CD, Tsai TM, Stebe KJ. Tip streaming from a drop in the presence of surfactants. *Phys Rev Lett.* 2001;87(4):048302.
24. Renardy YY, Renardy M, Cristini V. A new volume-of-fluid formulation for surfactants and simulations of drop deformation under shear at a low viscosity ratio. *Eur J Mech B/Fluids.* 2002;21(1):49-59.
25. Drumright-Clarke M, Renardy Y. The effect of insoluble surfactant at dilute concentration on drop breakup under shear with inertia. *Phys Fluids.* 2004;16(1):14-21.
26. James AJ, Lowengrub J. A surfactant-conserving volume-of-fluid method for interfacial flows with insoluble surfactant. *J Comput Phys.* 2004;201(2):685-722.
27. Martin DW, Blanchette F. Simulations of surfactant-laden drops rising in a density-stratified medium. *Phys Rev Fluids.* 2017;2(2):023602.
28. Xu JJ, Li Z, Lowengrub J, Zhao H. A level-set method for interfacial flows with surfactant. *J Comput Phys.* 2006;212(2):590-616.
29. De Langavant CC, Guittet A, Theillard M, Temprano-Coleto F, Gibou F. Level-set simulations of soluble surfactant driven flows. *J Comput Phys.* 2017;348:271-297.
30. Muradoglu M, Tryggvason G. A front-tracking method for computation of interfacial flows with soluble surfactants. *J Comput Phys.* 2008;227(4):2238-2262.
31. Dieter-Kissling K, Marschall H, Bothe D. Direct numerical simulation of droplet formation processes under the influence of soluble surfactant mixtures. *Comput Fluids.* 2015;113:93-105.
32. Shan X, Chen H. Lattice boltzmann model for simulating flows with multiple phases and components. *Phys Rev E.* 1993;47:1815-1819.
33. Shan X, Chen H. Simulation of nonideal gases and liquid-gas phase transitions by the lattice boltzmann equation. *Phys Rev E.* 1994;49: 2941-2948.
34. Chen L, Kang Q, Mu Y, He YL, Tao WQ. A critical review of the pseudopotential multiphase lattice boltzmann model: methods and applications. *Int J Heat Mass Transf.* 2014;76:210-236.

35. Kamali M, Sundaresan S, Van den Akker HEA, Gillissen J. A multicomponent two-phase lattice boltzmann method applied to a 1-d fischer–tropsch reactor. *Chem Eng J*. 2012;207:587-595.

36. Kamali M, Gillissen J, Van den Akker HEA, Sundaresan S. Lattice-boltzmann-based two-phase thermal model for simulating phase change. *Phys Rev E*. 2013;88(3):033302.

37. Zarghami A, Looije N, Van den Akker HEA. Assessment of interaction potential in simulating nonisothermal multiphase systems by means of lattice boltzmann modeling. *Phys Rev E*. 2015;92:023307.

38. Swift MR, Osborn W, Yeomans J. Lattice boltzmann simulation of nonideal fluids. *Phys Rev Lett*. 1995;75(5):830-833.

39. Orlandini E, Swift MR, Yeomans J. A lattice boltzmann model of binary-fluid mixtures. *EPL*. 1995;32(6):463-468.

40. Krüger T, Kusumaatmaja H, Kuzmin A, Shardt O, Silva G, Viggen EM. *Lattice Boltzmann for Advection-Diffusion Problems*. Cham, Switzerland: Springer; 2017.

41. Scarbolo L, Molin D, Perlekar P, Sbragaglia M, Soldati A, Toschi F. Unified framework for a side-by-side comparison of different multicomponent algorithms: lattice boltzmann vs. phase field model. *J Comput Phys*. 2013;234:263-279.

42. Chen H, Boghosian BM, Coveney PV, Nekovee M. A ternary lattice boltzmann model for amphiphilic fluids. *Proceed Royal Soc London A Math Phys Eng Sci*. 2000;456(2000):2043-2057.

43. Nekovee M, Coveney PV, Chen H, Boghosian BM. Lattice-boltzmann model for interacting amphiphilic fluids. *Phys Rev E*. 2000;62:8282-8294.

44. Skartlien R, Furtado K, Sollum E, Meakin P, Kralova I. Lattice–boltzmann simulations of dynamic interfacial tension due to soluble amphiphilic surfactant. *Phys A Stat Mech Appl*. 2011;390(12):2291-2302.

45. Furtado K, Skartlien R. Derivation and thermodynamics of a lattice boltzmann model with soluble amphiphilic surfactant. *Phys Rev E*. 2010;81(6):066704.

46. Shardt O, Mitra SK, Derksen J. Simulations of charged droplet collisions in shear flow. *Chem Eng J*. 2016;302:314-322.

47. Sbragaglia M, Benzi R, Biferale L, Succi S, Sugiyama K, Toschi F. Generalized lattice boltzmann method with multirange pseudopotential. *Phys Rev E*. 2007;75:026702.

48. Skartlien R, Grimes B, Meakin P, Sjöblom J, Sollum E. Coalescence kinetics in surfactant stabilized emulsions: evolution equations from direct numerical simulations. *J Chem Phys*. 2012; 137(21):214701.

49. Skartlien R, Sollum E, Schumann H. Droplet size distributions in turbulent emulsions: breakup criteria and surfactant effects from direct numerical simulations. *J Chem Phys*. 2013;139(17):174901.

50. Lamura A, Gonnella G, Yeomans JM. A lattice boltzmann model of ternary fluid mixtures. *EPL*. 1999;45(3):314-320.

51. Van der Sman R, Van der Graaf S. Diffuse interface model of surfactant adsorption onto flat and droplet interfaces. *Rheol Acta*. 2006; 46(1):3-11.

52. Tóth GI, Kvamme B. Analysis of ginzburg-landau-type models of surfactant-assisted liquid phase separation. *Phys Rev E*. 2015;91(3): 032404.

53. Tóth GI, Kvamme B. Phase field modelling of spinodal decomposition in the oil/water/asphaltene system. *Phys Chem Chem Phys*. 2015; 17(31):20259-20273.

54. van der Sman R, Meinders M. Mesoscale models of dispersions stabilized by surfactants and colloids. *Adv Colloid Interface Sci*. 2014;211: 63-76.

55. González-Segredo N, Coveney PV. Self-assembly of the gyroid cubic mesophase: lattice-boltzmann simulations. *EPL*. 2004;65(6):795-801.

56. González-Segredo N, Coveney PV. Coarsening dynamics of ternary amphiphilic fluids and the self-assembly of the gyroid and sponge mesophases: lattice-boltzmann simulations. *Phys Rev E*. 2004;69(6): 061501.

57. Coveney PV, Fowler PW. Modelling biological complexity: a physical scientist's perspective. *J R Soc Interface*. 2005;2(4):267-280.

58. Chin, J., Coveney, P.V. Chirality and domain growth in the gyroid mesophase. In: *Proceedings of the Royal Society of London A: Mathematical, Physical and Engineering Sciences*; vol. 462. The Royal Society, 2006:3575–3600.

59. Harting J, Giupponi G, Coveney PV. Structural transitions and arrest of domain growth in sheared binary immiscible fluids and microemulsions. *Phys Rev E*. 2007;75(4):041504.

60. Ponce-Torres A, Montanero JM, Herrada MA, Vega EJ, Vega JM. Influence of the surface viscosity on the breakup of a surfactant-laden drop. *Phys Rev Lett*. 2017;118:024501.

61. McNamara GR, Zanetti G. Use of the boltzmann equation to simulate lattice-gas automata. *Phys Rev Lett*. 1988;61:2332-2335.

62. Bhatnagar PL, Gross EP, Krook M. A model for collision processes in gases. I. Small amplitude processes in charged and neutral one-component systems. *Phys Rev*. 1954;94:511-525.

63. Nourgaliev RR, Dinh TN, Theofanous TG, Joseph D. The lattice boltzmann equation method: theoretical interpretation, numerics and implications. *Int Multiphase Flow J*. 2003;29:117-169.

64. Succi S. *The Lattice Boltzmann Equation: For Fluid Dynamics and Beyond. Numerical Mathematics and Scientific Computation*. Great Britain: Clarendon Press; 2001. ISBN. ISBN:9780198503989.

65. He X, Shan X, Doolen GD. Discrete boltzmann equation model for nonideal gases. *Phys Rev E*. 1998;57:R13-R16.

66. Mazloomi M A, Chikatamarla SS, Karlin IV. Entropic lattice boltzmann method for multiphase flows. *Phys Rev Lett*. 2015;114: 174502.

67. Numerical investigation of droplet motion and coalescence by an improved lattice boltzmann model for phase transitions and multiphase flows. *Comput Fluids*. 2012;53:93-104.

68. Kupershtokh A, Medvedev D, Karpov D. On equations of state in a lattice Boltzmann method. *Comput Math Appl*. 2009;58(5):965-974. mesoscopic Methods in Engineering and Science.

69. Chen L, Kang Q, Tang Q, Robinson BA, He YL, Tao WQ. Porescale simulation of multicomponent multiphase reactive transport with dissolution and precipitation. *Int J Heat Mass Transf*. 2015;85: 935-949.

70. Chopard, B., Lagrava, D., Malaspinas, O., Ouared, R., Latt, J., Lovblad, K.O., Pereira-Mendes, V. A lattice boltzmann modeling of bloodflow in cerebral aneurysms. In: *V Eur Conf Comput Fluid Dyn ECCOMAS CFD*; vol 453, 2010:12.

71. Sbragaglia M, Belardinelli D. Interaction pressure tensor for a class of multicomponent lattice boltzmann models. *Phys Rev E*. 2013;88(1): 013306.

72. Meng X, Guo Z. Multiple-relaxation-time lattice boltzmann model for incompressible miscible flow with large viscosity ratio and high péclet number. *Phys Rev E*. 2015;92(4):043305.

73. d'Humières D. Multiple–relaxation–time lattice Boltzmann models in three dimensions. *Philos Trans Royal Soc London A Math Phys Eng Sci*. 2002;360(1792):437-451.

74. Cahn JW. On spinodal decomposition. *Acta Metall*. 1961;9(9): 795-801.

75. Tanaka H. Hydrodynamic interface quench effects on spinodal decomposition for symmetric binary fluid mixtures. *Phys Rev E*. 1995;51(2): 1313-1329.

76. Siggia ED. Late stages of spinodal decomposition in binary mixtures. *Phys Rev A*. 1979;20(2):595-605.

77. Koch S, Desai RC, Abraham FF. Dynamics of phase separation in two-dimensional fluids: spinodal decomposition. *Phys Rev A*. 1983; 27(4):2152-2167.

78. Rogers T, Elder K, Desai RC. Numerical study of the late stages of spinodal decomposition. *Phys Rev B*. 1988;37(16):9638-9649.

79. Osborn W, Orlandini E, Swift MR, Yeomans J, Banavar JR. Lattice Boltzmann study of hydrodynamic spinodal decomposition. *Phys Rev Lett*. 1995;75(22):4031-4034.

80. González-Segredo N, Nekovee M, Coveney PV. Three-dimensional lattice-boltzmann simulations of critical spinodal decomposition in binary immiscible fluids. *Phys Rev E*. 2003;67(4):046304.

81. Chin J, Coveney PV. Lattice Boltzmann study of spinodal decomposition in two dimensions. *Phys Rev E*. 2002;66(1):016303.

82. Falcucci G, Bella G, Shiatti G, Chibbaro S, Sbragaglia M, Succi S. Lattice Boltzmann models with mid-range interactions. *Commun Comput Phys*. 2007;2:1071-1084.

83. Chibbaro S, Falcucci G, Chiatti G, Chen H, Shan X, Succi S. Lattice boltzmann models for nonideal fluids with arrested phase-separation. *Phys Rev E*. 2008;77:036705.

84. Dong H, Carr WW, Morris JF. An experimental study of drop-on-demand drop formation. *Phys Fluids*. 2006;18(7):072102.